Wavelength dependence of femtosecond laser-induced breakdown in water and implications for laser surgery

Norbert Linz, Sebastian Freidank, Xiao-Xuan Liang, and Alfred Vogel

Phys. Rev. B **94**, 024113 — Published 18 July 2016

DOI: 10.1103/PhysRevB.94.024113

Wavelength dependence of femtosecond laser-induced breakdown in water, and implications for laser surgery

Norbert Linz[1], Sebastian Freidank[1], Xiao-Xuan Liang[1,2], and Alfred Vogel[1]*

1) *Institut für Biomedizinische Optik, Universität zu Lübeck, Peter-Monnik Weg 4,*
23562 Lübeck, Germany

2) *Institute of Biomedical Analytical Technology and Instrumentation, School of Life Science and*
Technology, Xi'an Jiaotong University, Xi'an 710049, P. R. China

The wavelength dependence of the threshold for femtosecond optical breakdown in water provides information on the interplay of multiphoton, tunneling and avalanche ionization, and is of interest for parameter selection in laser surgery. We measured the bubble threshold from UV to near-IR wavelengths and found a continuous decrease of the irradiance threshold with increasing wavelength λ. Results are compared to the predictions of a numerical model that assumes a bandgap of 9.5 eV and considers the existence of a separate initiation channel via excitation of valence band electrons into a solvated state followed by rapid upconversion into the conduction band. Fits to experimental data yield an electron collision time of ≈ 1 fs, and an estimate for the capacity of the initiation channel. Using that collision time, the breakdown dynamics was explored up to λ = 2 µm. The irradiance threshold first continues to decrease but levels out for wavelengths longer than 1.3 µm. This opens promising perspectives for laser surgery at wavelengths around 1.3 µm and 1.7 µm, which are attractive because of their large penetration depth into scattering tissues.

PACS numbers: 79.20.Ds, 79.20.Ws, 42.62.Fi, 42.62.Be

77.22.Jp	Dielectric breakdown
79.20.Ds	Laser beam impact phenomena
79.20.Ws	Multiphoton absorption
42.62.Be	Biological and medical laser applications

1. INTRODUCTION

Focused femtosecond (fs) laser pulses offer the potential of precisely tunable nonlinear energy deposition in nominally transparent dielectrics. More specifically, femtosecond laser-induced optical breakdown in water and aqueous media enables to perform highly precise surgery on cells [1-3] and within transparent biological tissues [4-8]. The dependence of optical breakdown thresholds on laser parameters provides information about breakdown mechanisms such as the interplay of strong-field ionization (SFI) and avalanche ionization (AI) [9-14], as well as about the band structure of the breakdown medium and the mechanisms of breakdown initiation [15,16]. Detailed knowledge of the parameter dependence of breakdown thresholds is, furthermore, important for material processing and laser surgery.

SFI consists of multiphoton ionization (MPI) and tunneling ionization (TI). The relative significance of AI compared to SFI is still a matter of debate. This question has been experimentally addressed by studying the pulse duration dependence of the breakdown threshold, I_{th}, [11-13,17-21] or of focal transmittance [22], by investigating the temporal dynamics of free electron density at individual laser parameters via spectral interferometry [23-28] or time-resolved reflectivity measurements [29-31], or by exploring nonlinear absorption associated with femtosecond filamentation [32]. The interplay of AI and SFI was then assessed by comparing model predictions to the experimental data. However, the results were contradictory, as recently reviewed by Balling and Schou [14]. Positions reach from refuting the importance of AI in femtosecond breakdown [23,33,34], through acknowledgements of their moderate importance [35,36] to emphasizing their large importance [2,11,20-22,29,37-39] or even dominance [19,40-43]. The ongoing controversy defines a need for an extension of the experimental data base, accompanied by further refinements of breakdown modeling.

Besides the pulse duration dependence, also the wavelength dependence of the breakdown threshold, $I_{\mathrm{th}}(\lambda)$, contains valuable information on the breakdown dynamics [44]. Studies on $I_{\mathrm{th}}(\lambda)$ for IR nanosecond (ns) breakdown confirmed MPI initiation of AI [15,16]. In fs breakdown, seed electrons for AI are abundant, and SFI can contribute significantly to the free electron density reached at the end of the laser pulse. While TI exhibits no wavelength dependence because it depends on the laser field strength [34,45], the rate of MPI decreases with increasing wavelength, since the simultaneous absorption of an increasing number of photons is required to overcome the band gap. A leading role of MPI should, therefore, be reflected in an increase of I_{th} with increasing wavelength (λ). By contrast, the AI rate increases with λ, and I_{th} should decrease if AI dominates. Variations of the relative importance of MPI versus AI at wavelengths at which the order k of the multiphoton process increases could also result in a more complex shape of the $I_{\mathrm{th}}(\lambda)$ curve, such as steps whenever one more photon is needed for MPI [15,16,46]. Therefore, it is not sufficient to probe $I_{\mathrm{th}}(\lambda)$ at few individual wavelengths but a dense grid of data points needs to be collected over a large wavelength range to allow for meaningful conclusions.

The wavelength dependence of fs breakdown in band-gap solids has been investigated in several studies [29,34,46-48] but no detailed study on the wavelength dependence of fs breakdown in water is yet available. Olivié et al. measured I_{th} at the surface of corneal tissue at eight wavelengths between 800 nm and 1400 nm and interpreted the $I_{\mathrm{th}}(\lambda)$ trend using a breakdown model for water [49]. Consideration of the potential influence of biomolecules on the breakdown threshold is challenging and was not attempted in that study. Interpretation of $I_{\mathrm{th}}(\lambda)$ data for pure water would be more straightforward. In this paper, we determine the fs breakdown threshold in bulk water at 50 wavelengths between 335 nm and 1085 nm under diffraction-limited focusing conditions. Focusing at large numerical aperture (NA $\geq$ 0.8) avoids nonlinear beam propagation effects that could distort the threshold determination [50,51].

The experimental data are compared to model predictions based on the Keldysh theory of strong-field ionization and a modified Drude model for AI together with Rethfeld's multiple-rate-equation approach that accounts for the time-constraints of AI in fs breakdown [35]. Our model adopts recently gained insights about the band structure of water relevant for optical breakdown processes by assuming a bandgap of water of 9.5 eV together with a separate initiation channel via excitation of a valence band electron into a solvated state, followed by rapid excitation into the conduction band [16]. In the conduction band, the electron is quasi free, and we will thus use the term “free electron” synonymously with “conduction band electron”. Fitting model predictions to experimental data yields the Drude electron collision time, τ_{coll}, and the capacity of the initiation channel. Literature values for τ_{coll} used in previous studies on optical breakdown in transparent dielectrics vary by two orders of magnitude (from 0.11 fs in Ref. [49] to 23.3 fs in Ref. [52]). The present study will narrow the range of reasonable values for the effective Drude collision time in water, which is of great importance for future breakdown modeling.

Besides providing information on the breakdown mechanisms, knowledge of $I_{\text{th}}(\lambda)$ can guide parameter selection for fs laser surgery on cells and tissues. Cell surgery has mostly been performed using Ti-Sapphire lasers emitting at 800 nm [2,53] but can be even more precise with UV-A wavelengths [51]. Fs laser dissection in transparent tissues is already well established for creating corneal flaps in refractive laser surgery. Usually Ytterbium-based laser materials emitting at wavelengths around 1040 nm are employed [54] but UV wavelengths are also being tested to increase the cutting precision [55-58]. Great efforts are also undertaken to perform plasma-mediated surgery in scattering tissues such as skin, vocal cords, sclera, and brain [8,59-62]. Here, IR wavelengths around 1300 and 1700 nm seem to be optimally suited because they feature a large penetration depth due to a favorable combination of low scattering and moderate water absorption [49,59,63-65]. We use the Drude electron collision time obtained from fits in the range between 335 nm and 1085 nm to derive predictions for nonlinear energy deposition up to a wavelength of 2000 nm.

2. EXPERIMENTAL METHODS

The experimental setup for investigating the wavelength dependence of fs optical breakdown is presented in Fig. 1. Laser pulses are focused at high numerical aperture (NA) through long-distance water-immersion objectives (Leica, HCX APO L U-V-I, 63×/NA = 0.9 and 40×/NA = 0.8) into deionized and filtered (0.2 µm) water. The objectives are inserted into the wall of the water cell to enable aberration-free focusing of the laser pulses. The rear entrance pupil of each objective is slightly overfilled to create a uniform irradiance distribution corresponding to an Airy pattern in the focal plane. Breakdown is identified with the occurrence of bubble formation that is detected using the scattering of a continuous probe laser beam adjusted collinear and confocal with the pulsed laser beam. The scattering signal is detected by means of a fast photoreceiver (FEMTO, AC coupled, 25 kHz –200 MHz bandwidth) and a digital oscilloscope (Tektronix, DPO 70604). The scattering signal yields information on the time scale of the bubble oscillations, which is used to determine the maximum bubble radius, $R_{\max}$ [51]. This method provides a clear threshold criterion, since bubbles can be detected down to $R_{\max} \approx 150\,\mathrm{nm}$.

Laser pulses with tunable wavelength (335-1085 nm) are generated by a **t**raveling-wave **o**ptical **p**arametric **a**mplifier of **s**uperfluorescence (TOPAS) (Light Conversion, TOPAS 4/800). The TOPAS is pumped by a titanium sapphire fs laser (Spectra Physics Spitfire) emitting 460-µJ pulses of 120 fs duration at 795 nm wavelength and 1 kHz repetition rate. Coverage of a large wavelength range from UV to IR is achieved by generation of signal, idler, second-harmonic signal, second-harmonic idler, sum-frequency of pump and signal, sum-frequency of pump and idler, fourth-harmonic signal, and fourth-harmonic idler [66]. Maximum pulse energies vary between 3 µJ and 50 µJ in the investigated wavelength range. This is sufficient for a reliable breakdown threshold determination, since all threshold energies remain below 25 nJ due to the tight focusing of the laser beam. The TOPAS output is a mixture of the target wavelength and other contributions such as pump and idler. Six sets of dichroic mirrors are employed to separate the respective target wavelength from the other wavelengths over the entire tuning range.

For λ > 450 nm, spectra and pulse duration of the laser pulses are determined using a wavemeter (Ocean Optics, HR 2000), and an autocorrelator (APE, pulseCheck), respectively. Examples of spectra and autocorrelation traces are provided in the supplemental Fig. S1. Wavelengths below 450 nm are outside the autocorrelator's measurement range. Here, the pulse duration is set equal to the average pulse duration for λ > 450 nm, which is 250 fs. The duration of the TOPAS output fluctuates with wavelength, as shown in Fig. 2. To account for these variations, breakdown thresholds are normalized to the average over the whole range of measured pulse durations, as described further below.

A combination of two mechanical shutters (Uniblitz electronics, LS6) selects single pulses out of the 1 kHz pulse train. Wavelength-independent beam attenuation is achieved by a Fresnel-rhomb retarder in front of a Glan laser prism (both Karl Lambrecht Corporation). The energy in front of the microscope objectives is calibrated by a reference measurement for each wavelength, and the transmittance of the objectives is considered using data provided by the manufacturer. Breakdown energy thresholds (E_{th}) are determined by counting how frequently bubble formation occurs as the energy is increased from sub-threshold to super-threshold values. To eliminate the influence of energy fluctuations of the TOPAS output, the energy of each individual laser pulse is measured. Data are then binned into small energy intervals ($n \geq 15$) with > 20 events per interval, and fitted using the Gaussian error function. E_{th} corresponds to 50 % breakdown probability. The threshold irradiance I_{th} is then calculated using the equation

$$I_{th} = \frac{E_{th}}{\tau_L \, \pi \, (M^2 d / 2)^2} \times 3.73. \qquad (1)$$

Here τ_{L} denotes the laser pulse duration, M^2 is the beam quality parameter ($M^2 = 1.4$ according to manufacturer data for the TOPAS), and d is the diffraction-limited diameter of the Airy pattern arising from focusing a beam with top-hat profile, which is given by $d = 1.22\lambda/NA$. The factor 3.73 relates the average irradiance values within the pulse duration and focal spot diameter to the respective peak values that determine the onset of optical breakdown phenomena.

Measured threshold data are normalized to the average pulse duration (250 fs) via the experimentally determined pulse duration dependence of I_{th} for ultrashort-pulsed optical breakdown, which is $I_{\mathrm{th}} \propto \tau_{\mathrm{L}}^{-0.75}$ for pulse durations between 100 fs and 3 ps [20,67].

3. MODEL OF FEMTOSECOND-LASER-INDUCED PLASMA FORMATION

Since bubble formation defines the experimental breakdown threshold in aqueous media, the same threshold criterion must be used for modeling. This is comparatively easy for fs breakdown. Here only one set of free electrons is generated during the pulse because the recombination time is in the order of a few picoseconds [25,68], which is considerably longer than the laser pulse duration. Correspondingly, the thermalization of energy carried by the free-electrons through recombination and collisional energy transfer occurs mainly after the laser pulse. Therefore, the resulting temperature rise resulting in a phase transition can be assessed from the number density and average kinetic energy of free electrons at the end of the pulse [2,69].

As established previously, free electron generation is described using the full Keldysh model for SFI together with a Drude model for AI [2]. However, this approach is now used in conjunction with Rethfeld's multiple-rate-equation approach that considers the time constraints on AI in fs breakdown [35,36,38]. Furthermore, we consider recent insights about band structure and ionization pathways of water relevant for the optical breakdown.

3.1 Band structure and ionization pathways of water

Spectroscopic findings collected during the last two decades suggest that the band gap, E_{gap}, of liquid water is considerably larger than the value of 6.5 eV that has often been assumed in optical breakdown models for water. A band gap energy E_{gap} = 9.5 eV seems appropriate to consider both vertical and autoionization [16,70-73]. What was thought to be the band gap is actually an intermediate energy level between valence and conduction band, which plays a role mainly for breakdown initiation. Optical breakdown threshold spectroscopy of IR ns breakdown in water revealed two pronounced steps in the $I_{\text{th}}(\lambda)$ spectrum located at wavelengths for which an additional photon is required to provide the excitation energy E_{ini} for seed electron generation [9]. E_{ini} can be deduced from the separation of the steps and was found to be, on average, 6.6 eV [16]. This value lies slightly above the threshold for the generation of solvated electrons e_{aq}^{-}, E_{thsolv}, which is 6.4 eV [74-77]. That led to the conclusion that breakdown initiation proceeds via excitation of valence band electrons into the $\tilde{A}\ 1^1B_1$ absorption band, followed by their hydration and subsequent upconversion of e_{aq}^{-} into the conduction band as shown in Fig 3 (a).

Formation of e_{aq}^{-} at energies far below the conduction band requires the existence of pre-existing trap sites consisting of favorable local arrangements of water molecules that can accommodate the electron [77,78]. When an excited water molecule is located close to a trap site, an excess electron can be abstracted, prehydrate within ≈ 50 fs [79], and hydrate completely within less than 300 fs [73,79-81]. This process involves proton transfer to a neighboring water molecule resulting in the formation of a OH_{aq} radical and a hydronium ion $H_3O_{aq}^+$ [82-84]. An ideal trap corresponds to a tetrahedral conformation of four to six water molecules with their OH bonds directed towards the center [85,86] (Figs 3(b) and 3(c)). With increasing excitation energy E_{exc}, electrons can be accommodated also by initially less perfect configurations of water molecules, since part of E_{exc} is now available for rearranging the molecules in the process of electron abstraction.

The ultrafast hydration dynamics [79] and the long lifetime of solvated electrons [76] suggests that the breakdown initiation path via formation and upconversion of e_{aq}^- into the conduction band is favored compared to the path via light absorption by excited water molecules. H_2O^* exhibits a very short life time and a small absorption coefficient [87]. By contrast, both ground state and excited states (*p* states) of the solvated electron absorb well in a broad wavelength range from below 500 nm to above 1100 nm [76,80,88,89]. Therefore, only upconversion of e_{aq}^- is considered in the model and light absorption by excited water molecules is neglected.

Geminate recombination of e_{aq}^- with their $H_3O_{aq}^+$ hydronium counter-ions occurs on a time scale of tens of picoseconds [82] and plays no role for fs breakdown dynamics. Solvation of conduction band electrons becomes manifest only towards and after the end of the laser pulse [90,91], whereas during the pulse solvated electrons will be rapidly re-excited. Therefore, solvation of conduction band electrons has been neglected in the model.

3.2 Parameters governing breakdown initiation

When seed electrons produced by SFI are available, "local" avalanches arise around these electrons, which then merge into a "global" avalanche encompassing the entire focal volume [16,42,48]. The possible range of the seed avalanches decreases when the pulse duration is reduced and fewer doubling sequences can occur during a pulse. Correspondingly, the seed electron density ρ_{seed} necessary for the development of a homogeneous breakdown process must increase. While the exact choice of the ρ_{seed} value is crucial for IR ns breakdown, where it critically influences I_{th}, it is less decisive for the modelling of fs breakdown where seed electrons produced by SFI are abundant. Thus, ρ_{seed} is generally neglected in modeling fs breakdown, and we do the same in the present study.

The possible capacity of the initiation channel via formation and upconversion of e_{aq}^{-} into the conduction band is determined by the density and stability of pre-existing traps that can accommodate solvated electrons. The trap density, χ_{trap}, in liquid water at room temperature has been estimated to $0.73\times10^{19}\text{cm}^{-3}$ for E_{ini} = 6.42 eV [16]. It remains in the order of 10^{19}cm^{-3} up to 7.8 eV excitation energy, and increases rapidly thereafter. The trap density is 4-7 orders of magnitude higher than the critical seed electron density required for AI initiation in IR ns breakdown [16]. For ns breakdown, seed electrons will, therefore, not act back on the initiation channel. However, for ultrashort pulse durations at which seed electrons produced by SFI are abundant, the influence of free electrons on the initiation channel must be taken into account. Changes of the potential landscape induced by free electrons will likely disturb the local conformations of water molecules constituting the traps. Slight distortions of the trap sites will probably just increase the excitation energy required for e_{aq}^{-} formation but for sufficiently high free-electron density, the distortions will likely become so strong that the initiation channel vanishes. In our model, we assume that the initiation channel progressively decays while the free-electron density increases. The maximum number of free electrons that can be produced via the initiation channel is denoted $\rho_{ini,\max}$.

For UV wavelengths, many free electrons are produced via SFI already early during the laser pulse, as will be shown further below in section 4.2. Therefore, traps are distorted earlier during the pulse than at longer wavelengths, and E_{ini} must be higher to sustain the initiation pathway via pre-existing traps. For IR ns breakdown, Linz et al. obtained a good fit between measured and calculated $I_{\text{th}}(\lambda)$ curves assuming $E_{\text{ini}}(\lambda) = -(27/22400)\times\lambda + 7.59$ (with λ in nm and E_{ini} in eV) [16]. In the present study, we use the same $E_{\text{ini}}(\lambda)$ dependence and extrapolate it towards shorter wavelengths. For wavelengths > 990 nm, the fitting formula cannot be used because it yields E_{ini} values below the excitation threshold into the solvated state. Here, a constant value $E_{\mathrm{ini}} = E_{\mathrm{thsolv}} = 6.4$ eV is assumed.

3.3 Description of the breakdown dynamics

The dynamics of femtosecond breakdown is mainly determined by SFI and AI, whereas recombination and diffusion play little or no role for ultrashort laser pulses. Strong-field-ionization can either proceed through the initiation channel via excitation of valence band electrons into an intermediate level E_{ini} followed by subsequent upconversion, or it can occur as one step by ionization across the entire bandgap:

$$\left(\frac{d\rho_{SFI}}{dt}\right)=\left(\frac{d\rho_{ini}}{dt}\right)+\left(\frac{d\rho_{Egap}}{dt}\right)\text{, with} \tag{2}$$

$$\left(\frac{d\rho_{ini}}{dt}\right)=\eta_{SFI}(E_{ini})\times(1-\frac{\rho_{ini}}{\rho_{ini,\max}})\text{, and} \tag{3}$$

$$\left(\frac{d\rho_{Egap}}{dt}\right)=\eta_{SFI}\left(\tilde{\Delta}\right). \tag{4}$$

Here, the expressions $\eta_{SFI}(\;)$ represent the full Keldysh formulas (including multiphoton and tunneling effects) for photo-excitation into the intermediate E_{ini} – level and direct photo-ionization, respectively [2,92]. $\tilde{\Delta}$ denotes the effective ionization potential across the band gap that accounts for the oscillation energy of free electrons in strong electromagnetic fields, which is given by [92]

$$\tilde{\Delta}=\frac{2}{\pi}E_{gap}\frac{\sqrt{1+\gamma^2}}{\gamma}E\left(\frac{1}{\sqrt{1+\gamma^2}}\right)\text{, with}\quad \gamma=\frac{\omega}{e}\sqrt{\frac{m'cn\varepsilon_0 E_{gap}}{I}}. \tag{5}$$

The symbols ω and I denote the circular frequency and peak intensity of the electric laser field, e and m' are electron charge and reduced effective exciton mass, c is the vacuum speed of light, ε_0 the vacuum dielectric permittivity, and n is the refractive index of the medium at frequency ω. The reduced exciton mass m' is approximated by half of the mass m_c of conduction band electrons [10,33,35]. The term $E()$ denotes an elliptic integral of the second kind. The Keldysh parameter γ distinguishes SFI regimes: for $\gamma \ll 1$ tunneling dominates, while for $\gamma \gg 1$ MPI prevails; the transition occurs around γ = 1.5 (see Fig. 2 in Ref [2]).

Equation (3) is based on the assumption that the rate at which free electrons are produced via the initiation channel is fully determined by the rate at which excited water molecules at level E_{ini} are created. This simplification is justified by the fact that usually a high-order multiphoton process is needed to provide $E_{\text{ini}} \approx 6.6$ eV, whereas subsequent excitation of hydrated or solvated electrons into the conduction band is much easier. The second energy gap is smaller (3 eV) and contains intermediate energy levels (p-states of e^{-}_{aq}) that, like the ground state of the solvated electron, have a large absorption cross section even for low-energy photons [80,89,93]. Therefore, we neglect details of the upconversion and assume that all excess electrons are immediately elevated into the conduction band [16]. The depletion factor containing $\rho_{ini,\max}$ considers the finite capacity of the initiation channel that has been discussed in section 3.2. It should be noted that the initiation channel plays a significant role only for $\tau_{\text{L}} \geq 50$ fs when a substantial amount of hydrated and solvated electrons is available [79]. For shorter pulse durations, SFI must overcome the entire bandgap of 9.5 eV because of the small absorption cross section of H_2O*.

When conduction band electrons have become available through SFI, they gain kinetic energy through inverse Bremsstrahlung absorption of photons and can generate further free-electrons when their energy exceeds the critical energy required to cause impact ionization. To satisfy the conservation laws for energy and momentum, the kinetic energy of the impacting electron must be larger than the effective ionization potential $\tilde{\Delta}$ [94,95]. For a parabolic band gap, the minimum required energy is $E_{\text{crit}} = (3/2)\ \tilde{\Delta}$ [2,33,35,39]. The excess energy remaining after impact ionization is distributed among the collision partners. Thus, each quasi-free electron produced by impact ionization has to gain less energy than $1.5\tilde{\Delta}$ to reach E_{crit}. However, the average energy leading to an impact ionization event is likely somewhat larger than E_{crit} because the impact ionization rate increases with kinetic energy [33,96]. Therefore, we assume that the average energy gain required for a free electron to cause impact ionization is $1.5\tilde{\Delta}$ during the entire breakdown process. Impact ionization will follow shortly after an electron has gained $1.5\tilde{\Delta}$ [33,96].

If all conduction band electrons could take part in impact ionization, the average AI rate would be given by [35]:

$$\eta_{AI} = W_{1pt} \frac{\hbar\omega}{E_{crit}}, \tag{6}$$

where $W_{1\mathrm{pt}}$ is the intra-band one photon excitation rate that relates to the intra-band one photon absorption cross section σ_{1pt} by

$$\mathrm{W}_{1pt} = \sigma_{1pt} \frac{I}{\hbar\omega}. \tag{7}$$

However, only energetic electrons with $E > E_{\mathrm{crit}}$ are able to induce impact ionization. Therefore, impact ionization must be preceded by several collisions between electrons and heavy particles or phonons, during which the energy gain through inverse Bremsstrahlung absorption occurs [2,10,35]. The minimum number of collisional absorption events is

$$k' = \left\langle \frac{E_{crit}}{\hbar\omega} + 1 \right\rangle. \tag{8}$$

By implementing Eqs. (7) and (8) into Eq.(6), one can express η_{AI} in terms of σ_{1pt}, k' and photon flux $I/\hbar\omega$:

$$\eta_{AI} \approx \sigma_{1pt} \frac{1}{k'} \frac{I}{\hbar\omega} \tag{9}$$

The fact that excitation to E_{crit} requires a finite number of collisions imposes temporal constraints to AI. The microscopic processes involved have been followed in detail for crystalline solids by solving Boltzmann equations for the electrons and its collision partners [33,96-98] but this kinetic approach is numerically very expensive. Furthermore, the necessary material parameters are not yet known for water. Fortunately, Rethfeld has introduced a simplified model based on a set of rate equations, which keeps the essentials of the full kinetic approach but turns it into a more practical way [35]. The multiple-rate-equation model describes the excitation of the 'free' electrons using $k'+1$ discrete energy levels to represent the conduction band. Free electrons in lower energy levels are excited into higher energy levels in one-photon excitation steps occurring at rate $W_{1\mathrm{pt}}$. Impact ionization occurs only when they have reached the k'-th energy level. For a detailed description of the model composed of $k'+1$ ordinary differential equations, the reader is referred to Refs. [35,36,38].

The full set of rate equations is needed to describe the nonstationary electron distribution evolving in the course of very short laser pulses. At longer times, a transition to an asymptotic regime takes place for which the model can be simplified into a single-rate equation with a stationary AI rate. The asymptotic avalanche regime governs the breakdown dynamics during laser pulses that are considerably longer than the transition time [35,36]

$$t_{MRE} = \frac{1}{(\sqrt[k']{2}-1)\,\mathrm{W}_{1\mathrm{pt}}}\,. \tag{10}$$

The transition time t_{MRE} depends on irradiance, wavelength and on material parameters such as the band gap, and σ_{1pt}. The AI rate predicted by the asymptotic limit of the multiple-rate-equation model is

$$\eta_{AI,asymp}=\left(\sqrt[k']{2}-1\right)W_{1pt} \tag{11}$$

By applying the Laurent series to $\sqrt[k]{2}$, Eq. (11) can be approximated by [35]

$$\eta_{AI,asymp} \approx \ln 2\,\eta_{AI}\,. \tag{12}$$

Based on the Drude model, the intra-band one photon absorption cross section can be expressed as [10]

$$\sigma_{1PA} = \frac{\tau_{coll}}{\omega^2 \tau_{coll}{}^2 + 1} \cdot \frac{e^2}{c n_0 \varepsilon_0 m_c}\,, \tag{13}$$

with τ_{coll} denoting the time between momentum transfer collisions.

Combining Eqs. (6), (7), (11) and (13), we obtain the asymptotic AI rate as

$$\eta_{AI,asymp} \approx \ln 2\,\frac{\tau_{coll}}{\omega^2\,\tau_{coll}^2+1}\left(\frac{e^2\,I}{c\,n\,\varepsilon_0\,m_c\,(3/2)\,\tilde{\Delta}}\right). \tag{14}$$

Momentum transfer collisions entering the Drude model are collisions of electrons with phonons and heavy particles such as neutrals and ions [10,14,33,96-102]. Electron-electron collisions cannot contribute to τ_{coll} as both particles have the same effective mass. Therefore, their interaction conserves the total carrier momentum, which renders inverse Bremsstrahlung absorption impossible because the photon’s momentum cannot be accommodated [98,99].

Theoretical investigations of the respective collision rates for water are still lacking, and experimental investigations cannot easily distinguish between the individual contributions. Therefore, we treat τ_{coll} as free parameter in our model and use fits of the model to experimental results to determine the effective average τ_{coll} value for a free-electron density corresponding to the bubble threshold. Similar approaches have previously been followed by other researchers [19,26,32,103]. Reasonable fits can be expected for a range of τ_{coll} value in which the one photon absorption cross section is approximately proportional to the collision frequency. According to Eq. (13), this is the case if $\omega^2 \tau_{coll}{}^2 >> 1$, with $\omega^2 \tau_{coll}{}^2 \geq 1$ defining a lower limit. The latter condition is fulfilled for $\tau_{\mathrm{coll}} > 0.19$ fs at $\lambda = 350$ nm, and for $\tau_{\mathrm{coll}} > 0.56$ fs at 1050 nm.

The growth of free-electron density may be affected by diffusion and recombination losses. Diffusion out of the focal volume must be considered for ps and ns pulse durations but can be neglected in the description of fs breakdown. Possible recombination pathways include radiative electron-ion recombination [104], Auger recombination [95,104], non-radiative electron-ion recombination, electron neutral attachment with vibrational redistribution of the electron's energy [105], and electron solvation with subsequent decay of e_{aq}^{-} [76]. How important are these recombination pathways for the optical breakdown dynamics in water? Electron solvation becomes relevant only after the end of the laser pulse and will hardly influence the breakdown threshold [90]. Radiative recombination is pronounced in semiconductors [104] but plays little role in water breakdown. In fs breakdown, plasma radiation is faintly discernible only at pulse energies well above the bubble threshold, and even for ns breakdown, which is associated with bright blackbody-like plasma luminescence, the radiation was found to contain less than 10^{-3} % of the absorbed laser energy [67]. Auger recombination describes an energy-conserving interaction between two low-energy electrons and a hole upon which one electron recombines with the whole, and the other is excited onto a higher energy level. Its role for breakdown processes in silicon and SiO_2 has recently been investigated [97,98] but Auger processes have, to the best of our knowledge, not yet been reported for water breakdown. By contrast, non-radiative recombination of excess electrons with $H_3O_{aq}^{+}$ ions and electron attachment to neutral OH fragments is well investigated

[71,76,84,106]. Non-radiative recombination involves rapid dissipation of a large quantum of energy via vibrational relaxation and breakage of hydrogen bonds that is favored by the tight hydrogen bond network characteristic for liquid water [107-111]. At small excitation rates, ionization events are well separated from each other and recombination progresses mainly as geminate recombination within isolated ensembles of the three reaction partners e$^-$, $H_3O_{aq}^+$, and OH produced during ionization (Fig. 3a). Geminate recombination has a fixed time constant the value of which depends on the excitation energy that determines the ejection length of the excess electron [16,71]. At irradiance values leading to optical breakdown, ionization events are no longer isolated from each other, and cross recombination processes between photoproducts from independent ionization events dominate [83]. Under these circumstances, recombination is proportional to the square of free-carrier density because two types of free-carriers are involved in each event [10,105]. Therefore, we assume that recombination is proportional to ρ_c^2 and use an experimentally determined value for the recombination constant η_{rec}:

$$\left(\frac{d\rho_c}{dt}\right)_{rec} = -\eta_{rec} \times \rho_c^2, \quad \text{with} \quad \eta_{rec} = 1.8\times10^{-9}\,\mathrm{cm}^3/\mathrm{s}\ . \tag{15}$$

The η_{rec} value is the average of results obtained by inspecting the decay of plasma luminescence [105] ($\eta_{rec} = 2.0\times10^{-9}\,\mathrm{cm}^3/\mathrm{s}$) and by spectrally resolved reflection spectroscopy [25] ($\eta_{rec} = 1.6\times10^{-9}\,\mathrm{cm}^3/\mathrm{s}$).

We shall see below in section 3.4 that the electron density at the bubble threshold amounts to $\rho_{\mathrm{th}} = 1.8\times10^{20}$ cm^{-3}. The corresponding recombination time obtained based on Eq. (15) is 2.8 ps. Thus, recombination plays no significant role at the bubble threshold of femtosecond breakdown. However, this changes above threshold. For example, at $\rho_{\mathrm{c}} > 5\times10^{20}$ cm^{-3}, the time constant has dropped below 1 ps, and recombination will start to influence the breakdown dynamics.

The overall temporal evolution of conduction band electron density is given by

$$\left(\frac{d\rho_c}{dt}\right)=\left(\frac{d\rho_{SFI}}{dt}\right)+\eta_{AI,asymp}\times\rho_c-\eta_{rec}\times\rho_c^2\,, \tag{16}$$

when using the asymptotic model. For comparison, we also calculate the results predicted by the full multiple-rate-equation model. In the latter case, the full set of rate equations described in Ref. [35] is used instead of the term $\eta_{AI,asymp}$ from Eq. (14). The rate equation (16) is solved numerically for a Gaussian laser pulse using a Runge-Kutta method with adaptive step size control. The pulse duration τ_L is identified with the full width at half maximum. In order to evaluate the influence of MPI and AI, separate book-keeping is used for temporal evolution of ρ_{SFI} (total contribution from SFI), ρ_{ini} (excitation into an intermediate level followed by upconversion into the conduction band), and ρ_{Egap} (excitation across the entire bandgap) as given by Eqs. (2) - (4), respectively. The contribution of AI is $\rho_{AI} = \rho_c - \rho_{SFI}$.

3.4 Breakdown threshold criterion

The breakdown threshold is identified with bubble formation, i.e. with the temperature T_{th} that produces a phase transition at the focus center [2]. In fs breakdown, energy deposition is stress-confined and the phase transition is facilitated by thermoelastic tensile stress [2]. For near- IR laser pulses focused at NA = 0.8, a threshold temperature T_{th} = 440.7 K has been determined [51], corresponding to a temperature rise ΔT_{th} = 147.7 K above room temperature (293 K). For fs breakdown, ΔT_{th} can be connected to ρ_{th} by considering that the plasma energy density ε_{th} corresponds to the product of free electron density and average energy of a free electron. For electrons produced by AI, the latter is given by the sum of ionization potential $\tilde{\Delta}$ and average kinetic energy. Thus we have

$$\varepsilon_{th}=\rho_{th}(\tilde{\Delta}+\overline{E}_{kin})\,. \tag{17}$$

For estimating $\overline{E}_{kin}$, we assume that the energy distribution of electrons up to the impact ionization level is approximately flat. An average gain of 1.5 $\tilde{\Delta}$ required for impact ionization is consistent with a start energy of 0.5 $\tilde{\Delta}$ and an impact ionization level of 2 $\tilde{\Delta}$ [2], leading to $\overline{E}_{kin} = (5/4)\tilde{\Delta}$. The temperature rise after the laser pulse is

$$\Delta T=\frac{\varepsilon_{th}}{\rho_0\,C_p}\,, \tag{18}$$

where C_p is the heat capacity and ρ_0 the mass density of the medium. By combining (17) and (18), we obtain

$$\rho_{th} = \frac{\rho_0 \, C_p \, \Delta T}{(9/4)\tilde{\Delta}} . \qquad (19)$$

For T_{th} = 440.7 K, the threshold electron density is $\rho_{th} = 1.8\times10^{20}\,\mathrm{cm}^{-3}$, corresponding to an ionization degree of 0.27 %. (the number density of bound electrons that can be ionized is 6.68×10^{22} cm^{-3} [10]).

The electron density at the bubble threshold is considerably smaller than the critical electron density $\rho_{crit} = \omega_L^2 \, m_c \, \varepsilon_0 / e^2$ at which the plasma frequency equals the laser frequency ω_L [2,24] (ρ_{crit} amounts to $\approx 10^{22}$ cm^{-3} at λ = 335 nm and to $\approx 10^{21}$ cm^{-3} at 1085 nm). Since $\rho_{th} < \rho_{crit}$ for all wavelengths investigated, the optical properties are sufficiently well described by Eq. (13), and the changes in laser plasma coupling associated with the transition to electron densities $> \rho_{crit}$ [38,39,103] must not be considered. Furthermore, in bulk breakdown the free-carrier density remains comparatively small even above threshold because the breakdown front at which plasma formation is initiated moves upstream during the laser pulse [18,105,112].

4. RESULTS AND DISCUSSION

4.1 Wavelength dependence of breakdown thresholds

Figure 4(a) shows the experimental results on I_{th} (λ) for NA = 0.8 and NA = 0.9 together with bars marking the range between 10% and 90% breakdown probability. Experimental threshold data have been normalized to the average pulse duration $\tau_{\mathrm{L,avg}}$ = 250 fs as described at the end of section 2. Tabulated data from the threshold measurements before and after normalization are presented as supplementary information (Supplement Table 1). Figs. 4(b) and (c) present a comparison of experimental data averaged over both *NA*s with predictions of the full and asymptotic multiple-rate-equation model. The effective Drude collision time, τ_{coll}, and the capacity of the initiation channel, $\rho_{ini,\max}$, are used as free parameters.

Although the experimental data in Fig. 4(a) fluctuate by about ± 20 %, they clearly show a decrease of I_{th} with increasing wavelength. The modeling results in Fig. 4(b) reproduce this trend. However, the steps in the I_{th} (λ) curve predicted for wavelengths where the order of multiphoton excitation increases are not discernible in the experimental data. We attribute this to shortcomings of the complex TOPAS system resulting in experimental inaccuracies larger than the step size rather than to inadequacies of the breakdown model as will be discussed in the following.

The full Keldysh model employed for modeling strong-field ionization is widely accepted in the scientific community and used in most studies on fs breakdown. In agreement with this model, steps in the I_{th} (λ) curve have experimentally been observed for nanosecond breakdown, where SFI initiation determines I_{th} [15,16]. They were found also for femtosecond breakdown in a low-band gap material (TiO_2, with E_{gap} = 3.6 eV) at the transition from $k = 2$ to $k = 3$ [46]. The bandgap in water is larger than for TiO_2 and the corresponding step size at equal wavelengths is smaller since the step size decreases with increasing k. Therefore, the steps in water are more easily obscured by I_{th} fluctuations.

The fact that the I_{th} (λ) fluctuations in Fig. 4(a) are very similar for both *NA*s indicates that they are more likely related to variations of the laser emission rather than to imperfections of the technique for threshold determination. The laser beam quality (M^2) will differ between individual wavelength settings due to the complexity of the TOPAS system and the need for readjustment after wavelength tuning. Variations of M^2 by ±10-% will already change I_{th} by ± 20 %. Threshold fluctuations may also originate from hot spots in the laser beam if the distribution of these intensity peaks varies for different wavelengths. Furthermore, variable positive or negative chirps of the pulse could also affect the threshold determination [113]. Such influence has been observed when positive or negative chirps where imposed intentionally on 35-fs pulses with 18.7 nm transform-limited bandwidth [113]. However, in our case the average pulse duration is 250 fs, corresponding to a transform-limited bandwidth of only 2.6 nm. The small bandwidth limits the possible effect of chirping, and randomly arising chirps will usually be smaller than the outcome of intentional pulse shaping that prolonged the 35-fs pulse to 960 fs in Ref. [113]. Therefore, randomly arising chirps will probably have little influence on I_{th}.

The sharpness of the breakdown threshold will be affected by pulse-to-pulse variations of the transverse beam profile. Threshold sharpness is defined as $S = E_{\mathrm{th}}/\Delta E_{\mathrm{L}}$, where ΔE_{L} is the energy interval between 10 % and 90 % breakdown probability. For the TOPAS measurements, S is not as good as with fixed wavelengths, where values $S > 20$ are common. Only in 7% of the cases, $S > 20$ but in 16.3 % of the cases (n = 16), $S < 3$ (Supplement Table 1). Low threshold sharpness indicated by large bars in Fig. 4(a) was observed mainly at the edge of individual functioning regimes of the TOPAS, as already reported in previous studies [49].

Good agreement between model predictions and experimental results was obtained with an effective collision time $\tau_{\mathrm{coll}} = 0.9$ fs for the full multiple-rate-equation model and $\tau_{\mathrm{coll}} = 1.0$ fs for the asymptotic limit of the model [Fig. 4(b)]. A comparison of the best fit with the asymptotic model at $\tau_{\mathrm{coll}} = 1.0$ fs to results obtained with collision times of 0.5 fs and 1.5 fs shows that the fit depends critically on τ_{coll} [Fig. 4(c)]. A collision time of 1 fs is still within the validity limits for the Drude model discussed in section 3.3, which reaches down to $\tau_{\mathrm{coll}} \approx 0.5$ fs for $\lambda = 1050$ nm. With both modeling approaches, the best fit was obtained for $\rho_{ini,\max} = 10^{19}\mathrm{cm}^{-3}$, as will be further discussed in section 4.3.

To further substantiate the appropriateness of our modeling approach, we tested also another approach that predicts no steps in the $I_{\mathrm{th}}(\lambda)$ curve. Some researchers argued that MPI is quenched by collisions such that fs breakdown is driven by tunneling-initiated AI [40-43]. In that case, $I_{\mathrm{th}}(\lambda)$ should exhibit no discontinuities since the TI rate is wavelength-independent. The electron density produced by tunneling alone can be estimated from the result of the full Keldysh model at long wavelengths where MPI plays a negligible role. We have used the electron density at the bubble threshold predicted for $\lambda = 2000$ nm (10^{15} cm^{-3}, see section 4.4) as start value for modeling a breakdown process driven by tunneling-initiated AI. For that purpose, we used Eq. (16) without SFI term assuming that a seed electron density $\rho_{\mathrm{TI}} = 10^{15}$ cm^{-3} is present already at the beginning of the laser pulse. The results are presented in Fig. 5. With $\tau_{\mathrm{coll}} = 1$ fs, reasonable agreement with experimental data is observed for $\lambda > 900$ nm but for UV wavelengths, the threshold values are about 6 times too high. Thus, the $I_{\mathrm{th}}(\lambda)$ dependence is much too steep. With shorter collision time ($\tau_{\mathrm{coll}} = 0.3$ fs), a better match seems to be possible but this "improvement" is deceiving because now the condition $\omega^2 \tau_{coll}{}^2 \geq 1$ is not any more fulfilled at long wavelengths. With $\tau_{\mathrm{coll}} = 0.1$ fs, the above condition is violated in the entire wavelength range, and the results become completely non-physical. Thus, the full Keldysh theory provides significantly better fitting results than the alternative approach consistent with a smooth $I_{\mathrm{th}}(\lambda)$ dependence. This supports our interpretation that imperfections of the tunable laser system employed in the present study have precluded the experimental observation of steps in the $I_{\mathrm{th}}(\lambda)$ curve.

The overall agreement between the predictions of the full and asymptotic multiple-rate-equation models is very good because t_{MRE} is considerably shorter than the laser pulse duration in the entire wavelength range (t_{MRE} is 174 fs at 350 nm, and 22 fs at 1050 nm). The shape of the $I_{\mathrm{th}}(\lambda)$ curves differs slightly. Both models predict steps whenever the order k of the multiphoton process needed for excitation into the E_{ini} level or across the band gap changes. However, the full model predicts additional steps for changes of the number k' of one-photon excitation events that are needed to reach the impact ionization level. As mentioned above, such details cannot be resolved with the tunable laser system that was available in our study.

The τ_{coll} value obtained in the fitting procedure is strongly linked to the model assumptions on the electronic band structure of water. For a given threshold value, the assumption of a smaller band gap results in longer collision times because a slow avalanche will suffice to complete breakdown. Use of a simple rate equation without consideration of AI time constraints will also prolong τ_{coll}. Feit and coworkers obtained $\tau_{\text{coll}} \approx 3.3$ fs for 140-fs pulses using $E_{\text{gap}} = 6.5$ eV and a smaller critical energy for impact ionization than in our study ($E_{\text{crit}} = E_{\text{gap}}$ instead of $E_{\text{crit}} = (3/2)\ \tilde{\Delta}$) [103]. Dubietis et al. found $\tau_{\text{coll}} \approx 3$ fs using $E_{\text{gap}} = 6.5$ eV and a reduced cross section for MPI [32]. In both studies, a simple rate equation based on the Drude model was used to assess AI. Sarpe et al. and Winkler et al. evaluated time-resolved spectral interferometry data obtained at $\lambda = 785$ nm with the help of a Drude model using ionization coefficients and collision time as fitting parameters [26,28]. They obtained $\tau_{\text{coll}} \approx 1.6 \pm 0.3$ fs using $E_{\text{gap}} = 6.5$ eV [26] but the value of the effective collision time dropped to 0.18 fs (outside of the validity range of the Drude model) when they adjusted the band gap value to 8.3 eV without considering interband energy states [28]. Thus, it should be emphasized that the value $\tau_{\text{coll}} \approx 1$ fs obtained in the present study relates to the use of a band gap value of 9.5 eV in the breakdown model, the consideration of an initiation path via excitation into pre-existing traps at $E_{\text{ini}} \geq 6.4$ eV, and the employment of a multi-rate equation approach accounting for the time constraints of AI.

The procedure used for determining the effective collision time does not allow for a direct distinction between electron-phonon, electron-neutral, and electron-ion collisions. However, different collision mechanisms will dominate at different free-carrier densities [14]. Up to the bubble threshold, the free-electron density corresponds to an ionization degree of ≤ 0.27 % (section 3.4), and molecules in liquid water behave like those in a solid for vibrations above the Frenkel frequency [114]. Thus, electron-phonon collisions will prevail, and $\tau_{\text{coll}} \approx 1$ fs obtained by fitting model predictions to experimental bubble threshold data largely represents the electron-phonon collision time.

4.2 Interplay of Strong-field and avalanche ionization

The observed decrease of I_{th} with increasing λ indicates that AI plays an ever more important role for longer wavelengths. This becomes obvious by looking at the wavelength dependencies of MPI and AI rates presented in Fig. 6. All rates are calculated for the mean threshold irradiance $\overline{I}_{th}$=8.25*10^{16}W/m^2 obtained experimentally (Fig. 4). While the MPI rate decreases with increasing number of photons required for the multiphoton process, the AI rate increases for longer wavelengths. The tunneling rate exhibits no significant wavelength dependence [34,45]. Thus, I_{th} can drop with increasing λ only if AI dominates.

The interplay of SFI and AI is portrayed in more detail by the temporal evolution of free-electron density shown in Fig. 7 for UV, visible and IR wavelengths. At 347 nm [Fig. 7(a)], the initiation pathway is saturated, visible by the fact that ρ_{ini} rapidly reaches the maximum possible capacity of this channel, which for $\rho_{ini,\max}$ = 10^{19}cm^{-3} equals χ_{trap}. The contribution from SFI crossing the entire bandgap is large ($\rho_{\mathrm{Egap}} \approx 2.5*\rho_{\mathrm{Eini}}$). AI starts to play a role at the peak of the laser pulse when already a large number of free electrons have been generated. Since the AI rate is small at short wavelengths, the free electron density created by AI at the end of the pulse is just 3.6 times larger than the contribution from SFI. At 520 nm, the initiation pathway is still saturated but the SFI contribution from crossing the entire bandgap is now small compared to stepwise excitation via solvated states [Fig. 7(b)]. The relative importance of AI increases to $\rho_{\mathrm{AI}}/\rho_{\mathrm{SFI}}$ = 17. Finally, at 1040 nm, AI clearly dominates the breakdown process [Fig. 7(c)]. Although seed electrons are still abundant, with $\rho_{\mathrm{ini}} = 3.5 \times 10^{17}$ cm^{-3}, the initiation channel is not saturated any more (only 11.5 % of its maximum capacity is used), and AI provides 265 times more free electrons than SFI. At 1040 nm, AI starts to dominate the breakdown process already when ρ_{c} has exceeded a level of 10^{16} cm^{-3}, whereas at 347 nm, AI prevails only for $\rho_{\mathrm{c}} > 10^{19}$ cm^{-3}.

Figure 8 presents the simulated wavelength dependence of the ratio $\rho_{\mathrm{AI}}/\rho_{\mathrm{SFI}}$. The ratio increases stepwise whenever one more photon is needed for MPI, which is correlated also with a stepwise increase of I_{th} [Fig. 4 (b)]. The reduced MPI-contribution is compensated by an increased contribution of AI, which becomes possible through the higher threshold irradiance. Below 380 nm, E_{ini} can be reached by a 2-or 3 photon process, and the entire bandgap can also be crossed by a 3-photon process, which corresponds to a small $\rho_{\mathrm{AI}}/\rho_{\mathrm{SFI}}$ ratio. The step at 380 nm is due to an increase of the photon number required to cross E_{gap} from 3 to 4, as seen in Fig. 6. For $\lambda > 400$ nm, all steps in the $\rho_{\mathrm{AI}}/\rho_{\mathrm{SFI}}$ ratio are caused by an increase of the photon number needed to reach E_{ini} because MPI across the entire bandgap plays now only a negligible role [Figs. 7 (b) and (c)]. Below 350 nm, $\rho_{\mathrm{AI}}/\rho_{\mathrm{SFI}}$ is higher than between 350 nm and 380 nm. This is because for $\lambda < 350$nm a two photon process suffices to reach E_{ini}, which leads to early saturation of the initiation channel and provides a long time window for AI. Therefore, I_{th} drops (Fig. 4b) and the relative importance of AI increases.

Altogether, the breakdown process in water at 250 fs pulse duration can be well characterized as multiphoton-seeded avalanche ionization, with AI largely determining the bubble threshold I_{th}. It is interesting to note, that this characterization still applies for pulse durations well below 100fs. For $\lambda = 800$ nm, Sarpe et al. found that even at 35 fs pulse duration, AI accounts for more than 85% of the final free-electron density, which corresponds to $\rho_{\mathrm{AI}}/\rho_{\mathrm{SFI}} = 5.6$ [14,26]. At the same wavelength and $\tau_{\mathrm{L}} = 250$ fs, the ratio is $\rho_{\mathrm{AI}}/\rho_{\mathrm{SFI}} = 97$ (Fig. 8).

Assumptions on collision processes made in optical breakdown models strongly influence the outcomes on the relative importance of AI and SFI. In some classical theoretical studies on breakdown in SiO_2, attention was focused only on electron-phonon scattering, and electron-ion collisions, which become ever more relevant with increasing free-carrier density, were neglected [33,35,96]. As a consequence, the rate of free-carrier absorption in fused silica ablation and the role of AI were underestimated. For example, the $W_{1\mathrm{pt}}$ value for free-carrier absorption in fused silica employed originally by Rethfeld [35] corresponds to $\tau_{\mathrm{coll}} = 14.3$ fs in the Drude model as can be seen by comparing Eqs (7) and (13). This resulted in a much smaller contribution of AI than found in our present study on breakdown in water, which has a similar bandgap (9.5 eV) as fused silica (9 eV). For breakdown in fused silica at $\lambda = 500$ nm, $\tau_{\mathrm{L}} = 250$ fs, it was predicted that less than 5 % of the free electrons are generated by AI [35]. By contrast, with $\tau_{\mathrm{coll}} = 0.9$ fs that provides the best fit to our present experimental results, the multiple-rate-equation model predicts for the same wavelength and pulse duration that 15.7 times more electrons are produced by AI than by SFI. This picture is consistent with a later study by the Rethfeld group [38] in which electron-ion collisions were included and an effective electron collision time in the order of 1 fs was assumed, in accordance with experimental studies [19,99,101,115]. Now an avalanche-like behavior was found for irradiance conditions above the ablation threshold both with the multiple-rate-equation model and the kinetic approach [38]. In several recent studies on optical breakdown in large-band-gap solids, effective collision times ≤ 1 fs were used, and the results consistently revealed a large influence of AI, in agreement with our results on water [27,29,31,39,47].

4.3 Inter-band energy states and breakdown initiation

The interplay between SFI and AI is determined by the laser pulse duration, the band gap, and material parameters governing collisional interactions. Furthermore, intermediate energy states between valence and conduction band that exist in many types of transparent dielectrics also play an important role. If such states act as centers of reduced excitation energy as in water, they will facilitate breakdown but if they arise from self-trapping of excitons, the breakdown dynamics will, at least transiently, be slowed [27,38].

In water, the intermediate states consist of specific geometric arrangements of water molecules that are stabilized by relatively weak hydrogen bonds (see section 3.1). Therefore, they are labile and may be destroyed by the electric fields of conduction band electrons once their density exceeds a certain level (section 3.2). In order to assess the capacity of the initiation channel in water, we varied the parameter $\rho_{ini,\max}$ of the breakdown model, and compared the predicted wavelength dependence with the experimental I_{th} (λ) curve (Fig. 9). We see that for for $\rho_{ini,\max}$ = 10^{18}cm^{-3}, UV thresholds are too high and the slope of the I_{th} (λ) curve is too steep. For $\rho_{ini,\max}$ = 10^{20}cm^{-3}, the UV thresholds at wavelengths ≤ 340 nm are much too low. Thus, $\rho_{ini,\max}$ = 10^{19}cm^{-3}, equal to the trap density in liquid water, provides a good fit to experimental data. We conclude that about 10^{19} electrons per cm^3 can reach the conduction band through the initiation channel before it decays. Future studies will need to provide more data points at $\lambda < 340$ nm to consolidate this finding.

The free-electron density coming from the initiation channel drops with increasing wavelength, when the MPI rate decreases (Fig 7). According to our model, the initiation channel is saturated for λ < 530nm. For λ > 530 nm, the order of the multiphoton process necessary for reaching E_{ini} changes from $k = 3$ to $k = 4$, and $\rho_{\mathrm{ini,max}} / \chi_{\mathrm{trap}}$ drops below 60 %. With each increase of k, saturation drops further until it reaches values around 10 % for

$\lambda > 910$ nm, $k = 6$. The decrease of the seed electron density at longer wavelengths is compensated by an increasing strength of AI, as discussed in the previous section.

A decay of the initiation channel during the breakdown process, as hypothesized for water in the present study, is rather exceptional. It is a key factor in explaining the drop of breakdown thresholds with increasing λ in the short-wavelength range, which differs from the behavior in crystalline solids [29,47,48] and corneal tissue [49], where I_{th} increases with λ for $\lambda < 1000$ nm. The discrepancy maybe partially linked to differences in band gaps and pulse durations but we attribute it mainly to differences in number density, stability, and excitation kinetics of inter-band energy levels. The breakdown threshold at UV wavelengths will generally be reduced by conditions favoring MPI, such as a small band gap, short pulse durations, and inter-band energy levels. Correspondingly, the UV threshold was found to be smaller than at visible or IR wavelengths in simulations for $E_{\mathrm{gap}} = 5$ eV and $\tau_L = 100$ fs [39]. In our investigations, the band gap is larger (9.5 eV for water) and the pulse duration longer (250 fs), which already lessens the relative importance of MPI. It will be further quenched by a decay of the initiation channel during the breakdown process, as indicated by the simulations in Fig. 9.

In crystalline solids, inter-band energy states are more stable than in water and their number increases during breakdown. For example, during breakdown in SiO_2, which has a band gap of ≈ 9 eV [116], color centers are formed via rapid self-trapping of excitons occurring with a time constant of 150 fs [116-119]. Self-trapped excitons constitute an energy state $\approx$5.7 eV below the lower conduction band edge [38,116,119]. Although self-trapping will initially slow AI because it drains electrons from the conduction band, the situation changes when the STE density becomes saturated later during the pulse, or at higher irradiance [27]. Avalanche ionization is then no longer inhibited, and the inter-band energy states formed by the laser irradiation facilitate not only MPI but also boost AI [29,120]. The influence of inter-band energy levels is largest for $\lambda < 1000$ nm. At longer wavelengths, tunneling becomes increasingly important for seeding AI and differences between different breakdown media are less significant.

In transparent or semi-transparent tissues, centers of reduced excitation energy consist of biomolecules acting as electron donors. Electrons can be abstracted from certain aminoacides with energies similar or even smaller than those needed in pure water [121-123]. Such centers of reduced excitation energy are more stable than the pre-existing traps in water, and exist in large numbers. These features explain why the I_{th} (λ) dependency for cornea shows a similar threshold drop at shorter wavelengths as observed for crystalline solids [49].

Excess electrons originating from biomolecules may lower I_{th} in two ways: after upconversion into the conduction band, they can either directly seed AI, or their interaction with biomolecules can create reaction products exhibiting enhanced one- or multiphoton absorption. Several studies provided evidence that ultra-short pulsed laser-induced modification of biomolecules produces intermediates with different optical or electronic properties that accelerate further linear or nonlinear modification processes once their concentration is sufficiently high [124-129]. Thus, abstraction of excess electrons from biomolecules will either directly or indirectly enhance the photoionization channel of breakdown, which will lower the modification thresholds in biological media compared to the bubble formation threshold in pure water [2].

The possible amount of the threshold reduction by the presence of biomolecules is estimated in Fig. 10, where I_{th} (λ) dependencies for pure water are compared with curves corresponding to a 3- and 10-fold enhanced photoionization channel. Threshold changes are relatively small in the IR region where AI provides three or four orders or magnitude more free electrons than SFI but increase considerably for shorter wavelengths. At 330 nm, a 10-fold enhancement of ρ_{SFI} results in a 3-fold reduction of I_{th}. This trend is confirmed by experimental observations. For example, the threshold energy for bubble formation in mouse intestine by 355-nm 500-ps pulses focused at NA = 1.2 amounts to only one third of the respective value in water (33 nJ vs 103 nJ) [130]. Threshold measurements with IR and UV fs laser pulses in water with increasing concentration of bovine serum albumin showed that at a concentration of 10mg/ml, the bubble threshold decreased by 40% for 400 nm pulses, compared to only 7% at 800 nm [57,131].

Local variations in the concentration or composition of biomolecules that can provide excess electrons will be reflected in variations of the bubble threshold. According to the simulations in Fig. 10, such fluctuations will be more pronounced at short wavelengths than for IR breakdown. As a consequence, the size of laser effects produced by IR pulses of constant laser energy that are scanned across the tissue will likely be more uniform than effects produced at visible or UV wavelengths. Nevertheless, the minimum size of UV-induced effects is smaller due to the enhancement of the photoionization channel and the smaller focal volume.

4.4 *Consequences for femtosecond laser tissue surgery*

Fs laser surgery has been explored for various tissues such as cornea, lens, sclera, skin, vocal folds, and brain [4-8,62,132,133]. To date, surgery has mostly been performed at 800 nm and 1040 nm, the wavelengths of Titanium:Sapphire lasers and ytterbium-based lasers [6,8,54]. Recently UV-A pulses have been employed for flap cutting in corneal refractive surgery because the shorter wavelengths provides a better cutting precision due to the shorter plasma length [55-58,134] Furthermore, the collagen molecules in corneal tissue act as stable centers of reduced excitation energy in UV breakdown that lower the breakdown threshold and minimize mechanical side effects [58]. On the other hand, the wavelengths considerably longer than 1040 nm have been tested for plasma-mediated surgery in strongly scattering tissues such as sclera, skin and brain [59-61,63] and in edematous corneas [64].

Scattering decreases with increasing wavelengths but for $\lambda > 1$ µm, light penetration is increasingly affected by water absorption [135]. Xu and Wise determined the effective attenuation length for brain tissue given by the wavelength-dependent interplay of absorption and scattering, and found peaks around 1.3 µm and 1.7 µm [65]. Here, the optical penetration depth amounts to 330 µm and 480 µm, respectively, compared to only 130 µm at 800 nm. Thus, wavelengths of 1.3 µm and 1.7 µm are of great interest for laser surgery. Therefore, we use our model to derive predictions for nonlinear energy deposition in this parameter regime. For this purpose, the fit obtained in the wavelength region between 335 nm and 1085 nm was extrapolated up to 2000 nm using the same values for τ_{coll} and $\rho_{\mathrm{ini\_max}}$ as for the shorter wavelengths. It should be noted, however, that the choice of $\rho_{\mathrm{ini\_max}}$ is relevant only for UV breakdown (as shown in section 4.3) and has no influence on the modeling results in the extrapolation range. The results are presented in Fig. 11.

For $\lambda > 1$ µm, the bubble threshold I_{th} first continues to decrease with increasing λ (due to the growing efficiency of AI) but it levels out for $\lambda > 1200$ nm [Fig. 11(a)]. These model predictions for water are in good agreement with the experimental observation of a constant damage threshold in SiO_2 in the wavelength range between 1200 and 2200 nm reported by Grojo et al. [34]. For $\lambda > 1200$ nm, TI becomes increasingly important for the creation of seed electrons as indicated by the drop of the Keldysh parameter γ with wavelength that is presented in Fig. 11(b). The influence of tunneling is the reason, why SFI-produced seed electrons are abundant even at wavelengths around 2 µm [Fig. 11(c)]. Experimental evidence for the role of TI in initiating dielectric breakdown at mid-IR wavelengths has been provided in Ref. [48]. The $\rho_{\mathrm{SFI}}(I)$ curve in Fig. 11(c) does not distinguish between TI and MPI. Nevertheless, we can roughly assess their respective contributions by assuming that at $\lambda = 2$ µm ($\gamma \approx 1$) ρ_{SFI} is largely provided by TI. Since tunneling is wavelength independent [34,45], the contribution from TI at shorter wavelengths is approximately the same as at 2 µm. This yields ratios $\rho_{\mathrm{MPI}}/\rho_{\mathrm{TI}}$ of about 8000 at 347 nm, 275 at 800 nm, and $\rho_{\mathrm{MPI}}/\rho_{\mathrm{TI}} > 10$ for all wavelengths up to 1300 nm. Only at wavelengths > 2 µm, TI starts to dominate over MPI (for $\tau_L = 250$ fs).

The initial electron density predicted for 1050 nm, $\rho_{\mathrm{SFI}} = 3.5 \times 10^{17}$ cm^{-3}, is in good agreement with an estimate for large band-gap materials that was derived from the surface roughness of laser-produced nano-features produced at this wavelength [42]. However, our modeling results indicate that at 1050 nm ρ_{SFI} is produced mainly by MPI, whereas in [42] it is attributed to TI.

Grojo et al. concluded from the observation of a constant I_{th} value between 1200 nm and 2200 nm that the entire breakdown process in this wavelength region is dominated by TI and AI plays no role [34]. However, our modeling results show that TI alone does not suffice to produce breakdown and that the observed $I_{\mathrm{th}}(\lambda)$ behavior is well compatible with a prominent role of AI. The larger number k' of inverse Bremsstrahlung absorption events needed to produce impact ionization at longer wavelengths is compensated by an increase of the photon flux as becomes obvious from Eq. (9), together with a slight increase of the one–photon absorption cross section [Eq. (13)]. Therefore, the influence of AI first continues to increase with wavelength: we obtain $\rho_{\mathrm{AI}}/\rho_{\mathrm{SFI}}$ values of 1.48×10^4 at $\lambda = 1.7$ µm, and 5.29×10^4 at

$\lambda = 2.0$ µm. Since AI gains strength with increasing λ, a smaller seed electron density suffices to initiate homogeneous plasma formation, and ρ_{seed} can readily be provided by SFI. Finally, for wavelengths >> 2 µm, ρ_{seed} converges against a constant value produced by TI and the increase of the one photon cross section with wavelength saturates because $\omega^2\tau_{coll}^2$ drops well below 1 [Eq. (13)]. Since also the AI strength remains constant due to the balance between changes in *k*' and photon flux, I_{th} remains constant too.

For IR breakdown in biological tissues, similar trends should apply as for water because the relatively small seed electron density sufficient for initiating AI at IR wavelengths implies that biomolecules providing additional seed electrons have little influence on I_{th} (Fig. 10). The low optical breakdown threshold in water at wavelengths > 1 µm thus offers good prospects for fs laser surgery deep within scattering tissues. Figure 12 presents the wavelength dependence of the energy threshold for bubble formation, $E_{\mathrm{th}}(\lambda)$, both at the tissue surface and at various focusing depths *z* within the tissue. All data are calculated using Eq. (1) for τ_L = 250 fs, *NA* = 0.8 and M^2 = 1.4, assuming the same breakdown dynamics and thresholds as for water. $E_{\mathrm{th}}(\lambda)$ at the tissue surface relates directly to the $I_{\mathrm{th}}(\lambda)$ curve in Fig. 11(a) but considers the increase of spot size with growing wavelength. Estimates of E_{th} values at 200 µm, 500 µm, and 1000 µm focusing depth are obtained using data on the optical penetration length for brain tissue taken from Ref [65]. The difference in optical path lengths inside the tissue between central and peripheral rays of the tightly focused laser beams are neglected in this simple estimate.

For small focusing depths up to 200 µm, pulse energies required for surgery are smallest at wavelengths around 800 nm (emission of the Titanium:Sapphire laser). However, the energy minimum shifts to wavelengths around 1350 nm for *z* = 500 µm, and to the wavelength range around 1700 nm for z = 1 mm. For *z* = 500 µm, pulse energies between 0.2µJ and 0.3 µJ will probably suffice to perform surgery but for z = 1 mm pulse energies around 1 µJ may be needed even at the optimum laser wavelengths to achieve breakdown within cortical tissue. Achievable cutting depths and required cutting energies for tissues other than brain will vary depending on their scattering coefficients, vascularization, and pigmentation [135] but the values obtained in this study can serve as a landmark for parameter selection.

5. CONCLUSIONS

The wavelength dependence of the threshold for femtosecond optical breakdown in water at ≈250 fs pulse duration was investigated by measuring the threshold for bubble formation at 50 wavelengths between 335 nm and 1085 nm under diffraction-limited focusing conditions. We found a continuous decrease of I_{th} with increasing wavelength. Experimental results were compared to model predictions based on the Keldysh theory of SFI and a modified Drude model for AI together with a multiple-rate-equation approach that accounts for the time-constraints of AI in fs breakdown [35]. The model assumes a bandgap of water of 9.5 eV and the existence of a separate initiation channel via a solvated electron state that is quenched at high conduction band electron densities when the local conformations of water molecules constituting the traps are disturbed.

Good agreement between model predictions and experimental $I_{\mathrm{th}}(\lambda)$ data was obtained with an effective Drude collision time of $\tau_{\mathrm{coll}} = 0.9$ fs when the full multiple-rate-equation model was used, and $\tau_{\mathrm{coll}} = 1$ fs when the computationally less expensive asymptotic limit of the model for fully developed avalanche ionization was employed. The value of τ_{coll} is of major importance for obtaining a realistic picture of the interplay between SFI and AI. Furthermore, together with wavelength and irradiance, it determines the transition time t_{MRE} to the asymptotic regime in which AI can be described by a single rate equation. A value of $\tau_{\mathrm{coll}} = 1$ fs implies that for breakdown in water by 250-fs pulses, the asymptotic model can be used in the entire wavelength range investigated in this study.

The decrease of I_{th} with increasing λ indicates that AI plays a dominant role in the optical breakdown process because the AI rate becomes more effective for longer wavelengths whereas the MPI rate decreases with increasing number of photons required for MPI, and tunneling exhibits no significant wavelength dependence. According to the model calculations, the ratio of the free-electron densities provided by AI and SFI increases from $\rho_{\mathrm{AI}}/\rho_{\mathrm{SFI}} = 3.6$ at 350 nm to $\rho_{\mathrm{AI}}/\rho_{\mathrm{SFI}} = 265$ at 1050 nm and 5.3×10^4 at 2000 nm. Thus, breakdown proceeds as multiphoton-seeded avalanche ionization, with AI determining I_{th}.

Steps in the $I_{\mathrm{th}}(\lambda)$ dependence predicted by the breakdown model at wavelengths where one more photon is needed for MPI could not be discerned experimentally because the scattering of the $I_{\mathrm{th}}(\lambda)$ data exceeded the predicted height of the steps. This scatter and the small threshold sharpness at some wavelengths were caused by imperfections of the tunable laser system. Exploration of the fine structure of the $I_{\mathrm{th}}(\lambda)$ dependence remains a challenge that can be met only with improved laser technology.

The large value of the bubble threshold at UV wavelengths is indicative for a decay of the initiation channel in the course of the optical breakdown process. At short wavelengths, the free-electron density grows initially very fast by MPI but that induces changes of the potential landscape, which progressively distort the traps constituting an intra-band energy level at E_{ini}. The best fit to experimental $I_{\mathrm{th}}(\lambda)$ data was achieved for $\rho_{ini,\max} \approx \chi_{trap}$, i.e. by assuming that the maximum number density of electrons which can reach the conduction band through the initiation channel approximately resembles the density of pre-existing traps in liquid water under normal conditions, $\chi_{\mathrm{trap}} \approx 10^{19}$ cm^{-3}.

The $I_{\mathrm{th}}(\lambda)$ dependence observed for water differs from that in crystalline solids, where I_{th} increases with wavelength for $\lambda < 1000$ nm. This discrepancy can be explained by differences in the kinetics of inter-band energy states. While centers of reduced excitation energy fade away during the breakdown process in water, new centers are created by self-trapping of excitons in dielectric solids. Also in cells and tissues, biomolecules constitute fairly stable centers of reduced excitation energy. Therefore, the UV breakdown threshold in tissue is considerably lower than in water.

In UV-A breakdown, MPI contributes a considerable fraction of the final free-electron density both in water and biological tissues. Therefore, local variations of the density of centers of reduced excitation energy caused by inhomogeneities can strongly influence the breakdown threshold. By contrast, in IR breakdown AI provides three or four orders or magnitude more free electrons than SFI. As a consequence, additional seed electrons from biomolecules have little influence on the breakdown dynamics, and the breakdown threshold fluctuates less.

IR wavelengths around 1300 and 1700 nm are of great interest for laser surgery within scattering tissues due to a favorable combination of low scattering and moderate water absorption. Therefore, we used the model parameters obtained from fitting our experimental $I_{\mathrm{th}}(\lambda)$ data to derive predictions for nonlinear energy deposition up to a wavelength of 2000 nm. Up to λ = 1300 nm, MPI provides at least 10 times more seed electrons than tunneling. However, while the influence of MPI ceases for longer wavelengths, the contribution of tunneling remains approximately constant and guarantees the availability of seed electrons even at λ = 2 µm or larger. The strength of AI first continues to increase with wavelength and then remains approximately constant for λ > 2 µm where the influence of increasing k' and photon flux balance each other. Since with increasing λ the strength of both SFI (in the form of TI) and AI converge against constant levels, the bubble threshold assumes an approximately constant and low level for λ > 1.3 µm. This model prediction offers good prospects for fs laser surgery deep within scattering tissues.

ACKNOWLEDGMENT

This work was supported by U.S. Air Force Office of Scientific Research grants FA 8655-05-1-3010 and FA9550-15-1-0326, by Deutsche Forschungsgemeinchaft grant VO-470/14-2, and by Possehl Stiftung Lübeck. We thank Kristian Werelius and Boris Chichkov at Laser Center Hannover for providing access to the Spectra Physics Spitfire system that was used as pump laser for the TOPAS system.

---

* Corresponding author: vogel@bmo.uni-luebeck.de

FIGURE CAPTIONS

Fig. 1 Experimental setup for investigating the wavelength dependence of fs laser-induced breakdown in water. For details see text.

Fig. 2 Pulse durations $\tau_L(\lambda)$ of the TOPAS system in the wavelength range between 450 nm and 1085 nm. Wavelengths below 450 nm were outside the autocorrelator's measurement range. The averaged pulse duration above 450 nm is $\tau_{L,avg} = 250$ fs.

Fig. 3 (a) Ionization and geminate recombination pathways in liquid water as proposed in Ref. [16]. For large excitation energies, ionization proceeds via vertical ionization ($E_{exc} \geq 11$ eV) or autoionization ($E_{exc} \geq 9.5$ eV), while for $E_{exc} < 9.5$ eV, ionization is possible only as a two-step process involving solvated electron creation followed by upconversion of e^-_{aq} into the conduction band. The latter process competes with geminate recombination, especially at pulse durations longer than $\tau_{gemrec} \approx 60$ ps. (b), (c) Tetrahedral conformations of water molecules hosting a solvated electron. Reprinted with permission from Ref. [86], supporting information Fig. S7.1. Copyright (2015), American Chemical Society. The constellation with lowest potential energy is that in (b). Randomly formed cavity-like molecular conformations like that in (b) and (c) can act as traps promoting the abstraction of an electron from an excited water molecule. Deviations from these constellations require higher excitation energies for trap occupation, since part of E_{exc} is now required for conformation changes.

Fig. 4 Wavelength dependence of the optical breakdown threshold I_{th} (λ) for fs laser pulses. (a) Experimental data normalized to the average pulse duration of $\tau_L = 250$ fs for both investigated numerical apertures, $NA = 0.8$ and $NA = 0.9$. The bars mark the irradiance range between 10% and 90% breakdown probability. (b) Best fit of model predictions for I_{th} (λ) to the experimental data averaged over both NAs. Parameters used for the calculations are: $\tau_L = 250$ fs, $E_{gap} = 9.5$ eV, $\rho_{ini,max} = 10^{19}$ cm^{-3}, and E_{ini} (λ) as described in section 3.2. The effective collision time was $\tau_{coll} = 0.9$ fs with the full multiple-rate-equation model, and $\tau_{coll} = 1.0$ fs with the asymptotic limit of the model (MRE$_{asymp}$). (c) Plots of results obtained with the asymptotic model for collision times between 0.5 fs and 1.5 fs show that the fit depends critically on τ_{coll}.

Fig. 5 Simulations of I_{th} (λ) for a breakdown process driven by tunneling-initiated AI (TI+AI model). Breakdown thresholds are calculated by means of Eq. (16) without SFI term, assuming that TI produces an electron density $\rho_{\mathrm{TI}} = 10^{15}$ cm^{-3}, which is present from the beginning of the laser pulse. The electron collision time is varied in the range 0.1 fs < τ_{coll} < 1.0 fs. Results are compared to experimental data averaged over both *NA*s, and to the fit obtained using Eq. (16) with SFI term, representing the full Keldysh theory (SFI+AI model).

Fig. 6 Wavelength dependence of AI and MPI rates needed to reach E_{ini} and to cross E_{gap}. All rates are calculated for the mean threshold irradiance $\overline{I}_{th}$ =8.25×10^{16}W/m^{2} obtained experimentally (see Fig. 4).

Fig. 7 Temporal evolution of optical breakdown by 250-fs pulses of different wavelengths as predicted by the full multiple-rate-equation model for (a) 347 nm, (b) 520 nm, (c) 1040 nm. Each graph shows the total conduction band electron density ρ_{c} (all nonlinear absorption pathways including AI), the total contribution by ρ_{SFI} (plasma dynamics without AI arising from SFI), and the components constituting SFI. The contribution of AI to ρ_{c} is given by $\rho_{\mathrm{AI}} = \rho_{\mathrm{c}} - \rho_{\mathrm{SFI}}$. Strong-field-ionization includes a contribution ρ_{ini} from the initiation pathway (excitation into an intermediate level at E_{ini} followed by upconversion into the conduction band), and a contribution ρ_{Egap} from excitation across the entire bandgap. They are linked by $\rho_{\mathrm{ini}} = \rho_{\mathrm{SFI}} - \rho_{\mathrm{Egap}}$. In (b) and (c), ρ_{ini} is almost identical with ρ_{SFI} because ρ_{Egap} is very small. Therefore, $\rho_{\mathrm{ini}} \approx \rho_{\mathrm{SFI}}$ is not displayed separately. The free electron density at the bubble threshold is two orders of magnitude lower than the density ρ_{c} = 6.68×10^{22} cm^{-3} corresponding to full ionization [2,10].

Fig. 8 Ratio of free-electron density produced by AI to that created by SFI, $\rho_{\mathrm{AI}}/\rho_{\mathrm{SFI}}$, plotted as a function of wavelength for 250-fs laser pulse duration. Calculations were performed using the asymptotic limit of the multiple-rate-equation model. For λ > 400 nm, steps in the $\rho_{\mathrm{AI}}/\rho_{\mathrm{SFI}}(\lambda)$ curve correspond to changes of the order of the multiphoton process required to reach E_{ini} (the respective orders are indicated by the numbers in the figure). For λ < 400 nm, changes in the order of MPI excitation across the entire bandgap also play a role.

Fig. 9 Predictions of the asymptotic model for I_{th} (λ) assuming different capacities of the initiation channel in the range 10^{18} cm^{-3} < $\rho_{\mathrm{ini,max}}$ < 10^{20} cm^{-3}. The pulse duration is τ_L = 250 fs.

Fig. 10 Simulation of I_{th} (λ) assuming different strengths of the photoionization channel. The curve for ρ_{SFI} = 1 represents the situation in pure water, whereas the 3- and 10-fold enhancement of the photoionization channel serves as simple model for the possible influence of biomolecules that introduce additional inter-band states, which will facilitate MPI. The enhancement is simulated by multiplying the term $(d\rho_{SFI} / dt)$ in Eq. (16) by a factor of 3 or 10, respectively.

Fig. 11 Predictions for the wavelength dependence of fs laser breakdown in water up to $\lambda = 2$ µm, for τ_L = 250 fs. (a) Irradiance threshold for bubble formation, (b) Keldysh parameter at the bubble threshold, (c) Free-electron density created by SFI.

Fig. 12 Calculated wavelength dependence of the pulse energy threshold E_{th} for fs laser breakdown in brain tissue at the tissue surface (z = 0) and different focusing depths. Calculations were performed for τ_L = 250 fs, NA = 0.8, and M^2 = 1.4 using the $I_{\mathrm{th}}(\lambda)$ data of Fig. 10 and data on optical penetration depth from Ref [65]. Breakdown dynamics and threshold temperature were assumed to be the same as for bubble formation in water.

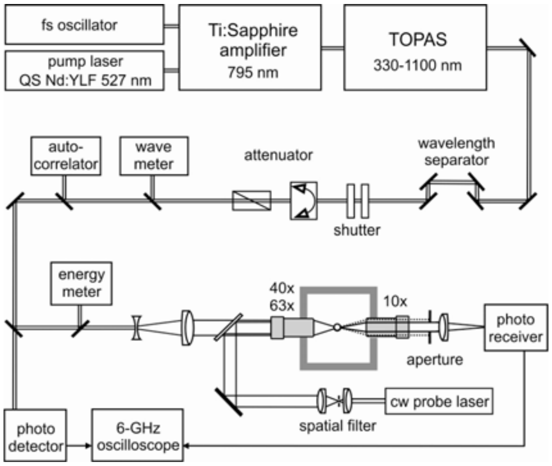
fs oscillator
pump laser
QS Nd:YLF 527 nm
Ti:Sapphire amplifier
795 nm
TOPAS
330-1100 nm
auto-correlator
wave meter
attenuator
wavelength separator
shutter
energy meter
40x
63x
10x
photo receiver
aperture
cw probe laser
spatial filter
photo detector
6-GHz oscilloscope

Figure 1

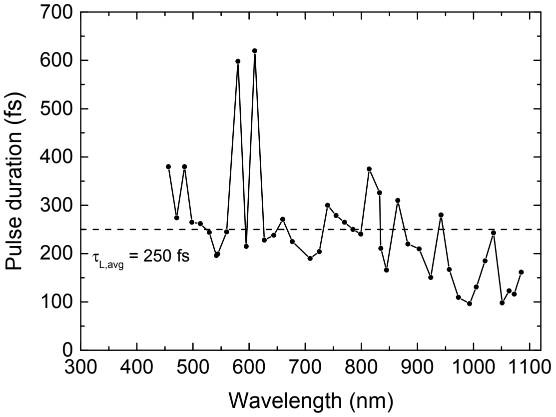
Pulse duration (fs)
0
100
200
300
400
500
600
700
300
400
500
600
700
800
900
1000
1100
Wavelength (nm)
$\tau_{L,avg}$ = 250 fs

Figure 2

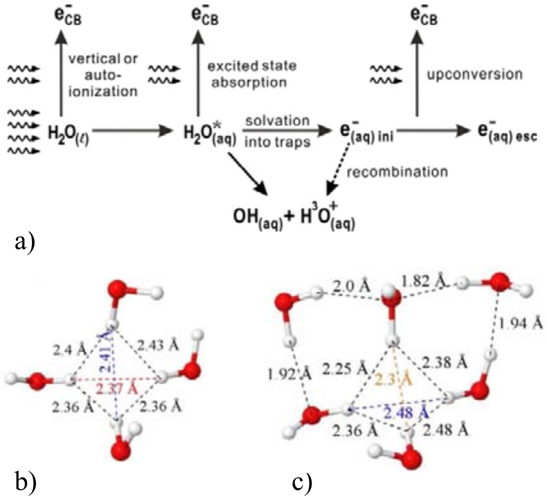
e⁻CB
vertical or auto-ionization
e⁻CB
excited state absorption
e⁻CB
upconversion
H2O(ℓ)
H2O*(aq)
solvation into traps
e⁻(aq) ini
e⁻(aq) esc
recombination
OH(aq) + H3O+(aq)
a)
2.4 Å
2.41 Å
2.43 Å
2.37 Å
2.36 Å
2.36 Å
b)
2.0 Å
1.82 Å
1.94 Å
1.92 Å
2.25 Å
2.3 Å
2.38 Å
2.48 Å
2.36 Å
2.48 Å
c)

Figure 3

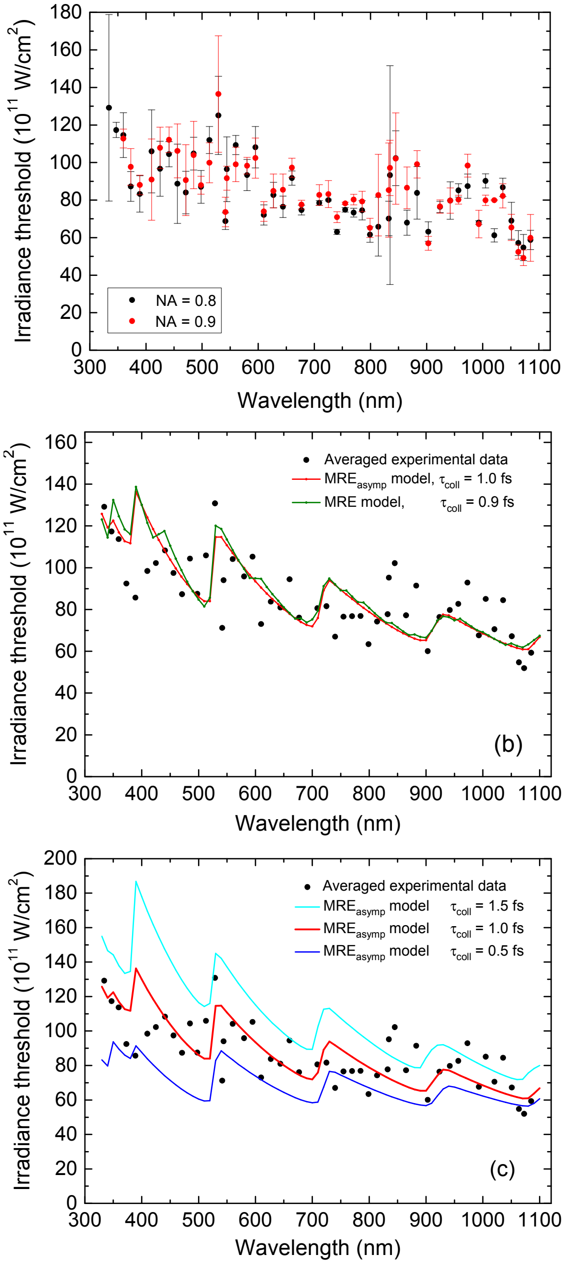
Irradiance threshold (10^{11} W/cm^2)
Wavelength (nm)
NA = 0.8
NA = 0.9
Averaged experimental data
MRE$_{asymp}$ model, τ_{coll} = 1.0 fs
MRE model, τ_{coll} = 0.9 fs
(b)
Averaged experimental data
MRE$_{asymp}$ model τ_{coll} = 1.5 fs
MRE$_{asymp}$ model τ_{coll} = 1.0 fs
MRE$_{asymp}$ model τ_{coll} = 0.5 fs
(c)

Figure 4

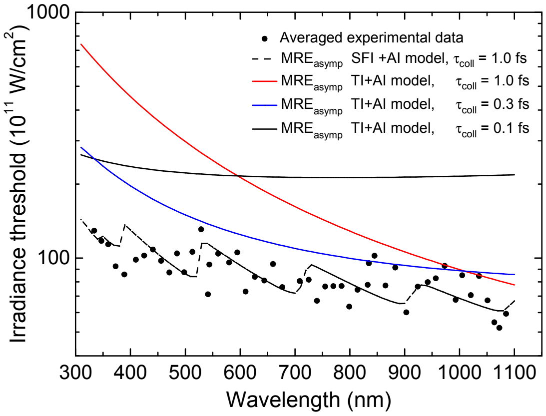

● Averaged experimental data
MRE$_{asymp}$ SFI +AI model, τ_{coll} = 1.0 fs
MRE$_{asymp}$ TI+AI model, τ_{coll} = 1.0 fs
MRE$_{asymp}$ TI+AI model, τ_{coll} = 0.3 fs
MRE$_{asymp}$ TI+AI model, τ_{coll} = 0.1 fs
Irradiance threshold (10^{11} W/cm^2)
1000
100
300
400
500
600
700
800
900
1000
1100
Wavelength (nm)

Figure 5

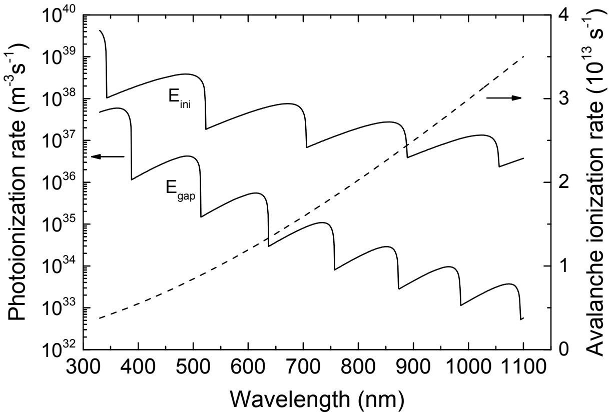
10^{40}
10^{39}
10^{38}
10^{37}
10^{36}
10^{35}
10^{34}
10^{33}
10^{32}
Photoionization rate ($m^{-3}s^{-1}$)
4
3
2
1
0
Avalanche ionization rate (10^{13} s^{-1})
300
400
500
600
700
800
900
1000
1100
Wavelength (nm)
E_{ini}
E_{gap}

Figure 6

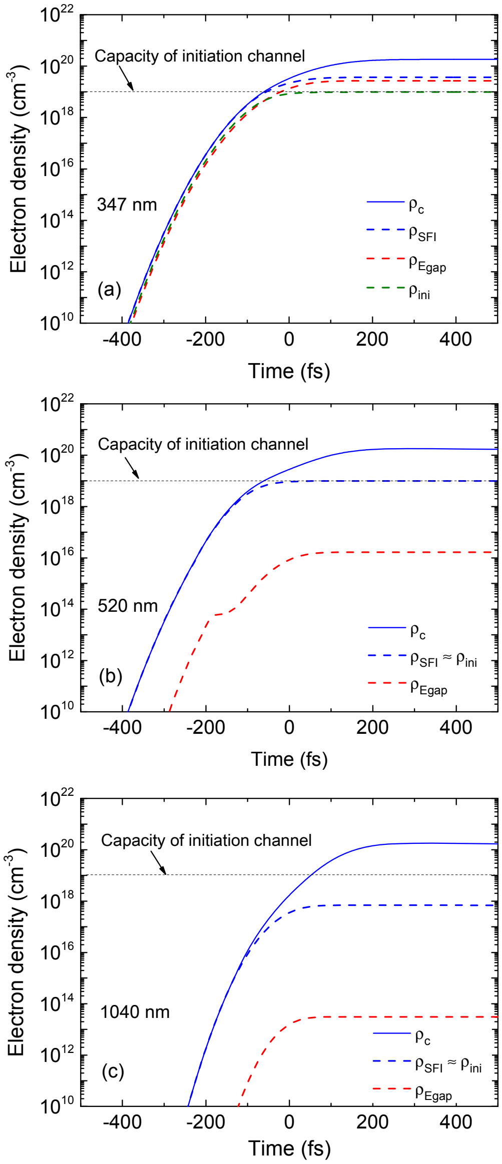

Capacity of initiation channel
347 nm
(a)
ρ_c
ρ_{SFI}
ρ_{Egap}
ρ_{ini}
Electron density (cm^{-3})
Time (fs)
Capacity of initiation channel
520 nm
(b)
ρ_c
$\rho_{SFI} \approx \rho_{ini}$
ρ_{Egap}
Electron density (cm^{-3})
Time (fs)
Capacity of initiation channel
1040 nm
(c)
ρ_c
$\rho_{SFI} \approx \rho_{ini}$
ρ_{Egap}
Electron density (cm^{-3})
Time (fs)
10^{10}
10^{12}
10^{14}
10^{16}
10^{18}
10^{20}
10^{22}
-400
-200
0
200
400

Figure 7

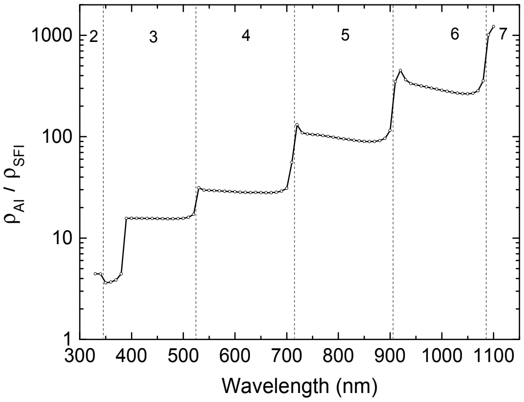
2
3
4
5
6
7
1000
100
10
1
ρ_{Al} / ρ_{SFI}
300
400
500
600
700
800
900
1000
1100
Wavelength (nm)

Figure 8

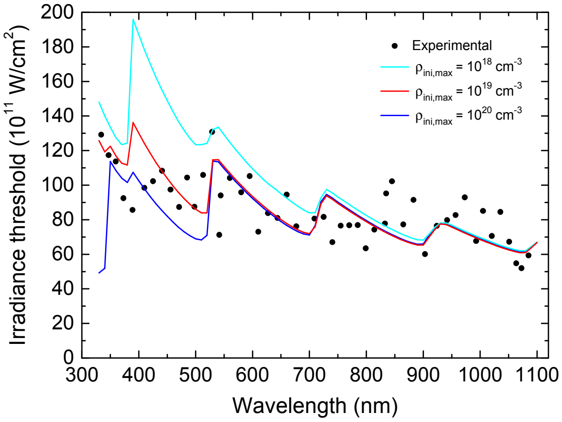
Irradiance threshold (10^{11} W/cm^2)
0
20
40
60
80
100
120
140
160
180
200
Wavelength (nm)
300
400
500
600
700
800
900
1000
1100
● Experimental
$\rho_{ini,max} = 10^{18}$ cm^{-3}
$\rho_{ini,max} = 10^{19}$ cm^{-3}
$\rho_{ini,max} = 10^{20}$ cm^{-3}

Figure 9

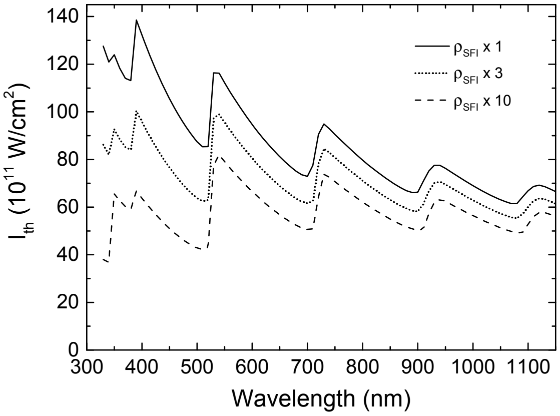

140
120
100
80
60
40
20
0
I_{th} (10^{11} W/cm^2)
300
400
500
600
700
800
900
1000
1100
Wavelength (nm)
ρ_{SFI} x 1
ρ_{SFI} x 3
ρ_{SFI} x 10

Figure 10

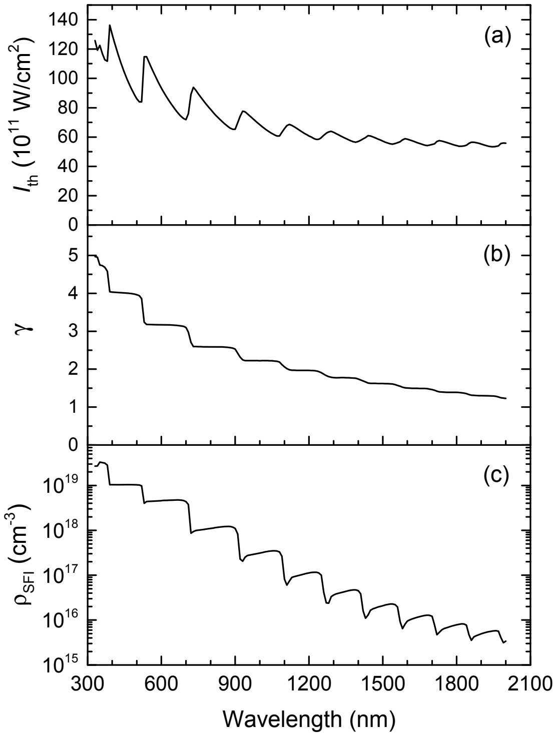
I_{th} (10^{11} W/cm^2)
140
120
100
80
60
40
20
0
(a)
γ
5
4
3
2
1
0
(b)
ρ_{SFI} (cm^{-3})
10^{19}
10^{18}
10^{17}
10^{16}
10^{15}
(c)
300
600
900
1200
1500
1800
2100
Wavelength (nm)

Figure 11

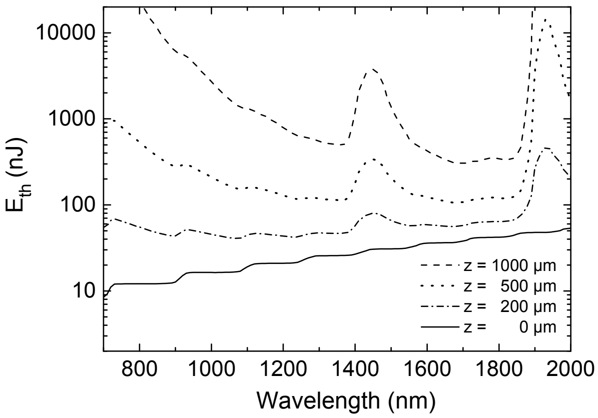
E_{th} (nJ)
10000
1000
100
10
800
1000
1200
1400
1600
1800
2000
Wavelength (nm)
z = 1000 µm
z = 500 µm
z = 200 µm
z = 0 µm

Figure 12

REFERENCES

1. K. Koenig, I. Riemann, P. Fischer, and K. H. Halbhuber, *Intracellular nanosurgery with near infrared femtosecond laser pulses*, Cell. Mol. Biol. **45**, 195 (1999).
2. A. Vogel, J. Noack, G. Huettman, and G. Paltauf, *Mechanisms of femtosecond laser nanosurgery of cells and tissues*, Appl. Phys. B. **81**, 1015 (2005).
3. P. Ronchi, S. Terjung, and R. Pepperkok, *At the cutting edge: Applications and perspectives of laser nanosurgery in cell biology*, Biol. Chem. **393**, 235 (2012).
4. A. Vogel, P. Schweiger, A. Frieser, M. Asiyo, and R. Birngruber, *Intraocular Nd:YAG laser surgery: damage mechanism, damage range and reduction of collateral effects.*, IEEE J. Quantum Electron. **26**, 2240 (1990).
5. T. Juhasz, F. H. Loesel, R. M. Kurtz, C. Horvath, J. F. Bille, and G. Mourou, *Corneal refractive surgery with femtosecond lasers*, IEEE J. Sel. Topics Quantum Electron. **5**, 902 (1999).
6. S. H. Chung and E. Mazur, *Surgical applications of femtosecond lasers*, J. Biophotonics **2**, 557 (2009).
7. D. V. Palanker, M. S. Blumenkranz, D. Andersen, M. Wiltberger, G. Marcellino, P. Gooding, D. Angeley, G. Schuele, B. Woodley, and M. Simoneau, *Femtosecond laser-assisted cataract surgery with integrated optical coherence tomography*, Sci. Transl. Med. **2**, 58ra85 (2010).
8. C. L. Hoy, O. Ferhanoglu, M. Yildirim, K. H. Kim, S. S. Karajanagi, K. M. C. Chan, J. B. Kobler, S. M. Zeitels, and A. Ben-Yakar, *Clinical ultrafast laser surgery: Recent advances and future directions*, IEEE J. Sel. Topics Quantum Electron. **20**(2014).
9. N. Bloembergen, *Laser-induced electric breakdown in solids*, IEEE J. Quantum Electron. **10**, 375 (1974).
10. P. K. Kennedy, *A first-order model for computation of laser-induced breakdown thresholds in ocular and aqueous media: Part 1 - Theory*, IEEE J. Quantum Electron. **31**, 2241 (1995).
11. B. C. Stuart, M. D. Feit, S. Herman, A. M. Rubenchik, B. W. Shore, and M. D. Perry, *Nanosecond-to-femtosecond laser-induced breakdown in dielectrics*, Phys. Rev. B **53**, 1749 (1996).
12. M. Lenzner, J. Kruger, S. Sartania, Z. Cheng, C. Spielmann, G. Mourou, W. Kautek, and F. Krausz, *Femtosecond optical breakdown in dielectrics*, Phys. Rev. Lett. **80**, 4076 (1998).
13. M. Mero, J. Liu, W. Rudolph, D. Ristau, and K. Starke, *Scaling laws of femtosecond laser pulse induced breakdown in oxide films*, Phys. Rev. B **71**(2005).
14. P. Balling and J. Schou, *Femtosecond-laser ablation dynamics of dielectrics: basics and applications for thin films*, Rep. Prog. Phys. **76**(2013).
15. C. W. Carr, H. B. Radousky, and S. G. Demos, *Wavelength dependence of laser-induced damage: Determining the damage initiation mechanisms*, Phys. Rev. Lett. **91**(2003).
16. N. Linz, S. Freidank, X. X. Liang, H. Vogelmann, T. Trickl, and A. Vogel, *Wavelength dependence of nanosecond infrared laser-induced breakdown in water: Evidence for multiphoton initiation via an intermediate state*, Phys. Rev. B **91**(2015).
17. P. K. Kennedy, S. A. Boppart, D. X. Hammer, B. A. Rockwell, G. D. Noojin, and W. P. Roach, *A first-order model for computation of laser-induced breakdown thresholds in ocular and aqueous-media: Part 2 - Comparison to experiment*, IEEE J. Quantum Electron. **31**, 2250 (1995).
18. A. Vogel, K. Nahen, D. Theisen, and J. Noack, *Plasma formation in water by picosecond and nanosecond Nd: YAG laser pulses - Part I: Optical breakdown at threshold and superthreshold irradiance.*, IEEE J. Sel. Topics Quantum Electron. **2**, 847 (1996).
19. P. P. Pronko, P. A. VanRompay, C. Horvath, F. Loesel, T. Juhasz, X. Liu, and G. Mourou, *Avalanche ionization and dielectric breakdown in silicon with ultrafast laser pulses*, Phys. Rev. B **58**, 2387 (1998).
20. J. Noack and A. Vogel, *Laser-induced plasma formation in water at nanosecond to femtosecond time scales: calculation of thresholds, absorption coefficients, and energy density*, IEEE J. Quantum Electron. **35**, 1156

(1999).

21. B. Chimier, O. Uteza, N. Sanner, M. Sentis, T. Itina, P. Lassonde, F. Legare, F. Vidal, and J. C. Kieffer, *Damage and ablation thresholds of fused-silica in femtosecond regime*, Phys. Rev. B **84**(2011).
22. P. P. Rajeev, M. Gertsvolf, P. B. Corkum, and D. M. Rayner, *Field dependent avalanche ionization rates in dielectrics*, Phys. Rev. Lett. **102**(2009).
23. F. Quere, S. Guizard, and P. Martin, *Time-resolved study of laser-induced breakdown in dielectrics*, Europhys. Lett. **56**, 138 (2001).
24. S. S. Mao, F. Quere, S. Guizard, X. Mao, R. E. Russo, G. Petite, and P. Martin, *Dynamics of femtosecond laser interactions with dielectrics*, Appl. Phys. A **79**, 1695 (2004).
25. C. Sarpe-Tudoran, A. Assion, M. Wollenhaupt, M. Winter, and T. Baumert, *Plasma dynamics of water breakdown at a water surface induced by femtosecond laser pulses*, Appl. Phys. Lett. **88**(2006).
26. C. Sarpe, J. Köhler, T. Winkler, M. Wollenhaupt, and T. Baumert, *Real-time observation of transient electron density in water irradiated with tailored femtosecond laser pulses*, New J. Phys. **14**, 075021 (2012).
27. L. Haahr-Lillevang, K. Waedegaard, D. B. Sandkamm, A. Mouskeftaras, S. Guizard, and P. Balling, *Short-pulse laser excitation of quartz: experiments and modelling of transient optical properties and ablation*, Appl. Phys. A **120**, 1221 (2015).
28. T. Winkler, C. Sarpe, N. Jelzow, L. Lasse H, N. Götte, B. Zielinski, P. Balling, A. Senftleben, and T. Baumert, *Probing spatial properties of electronic excitation in water after interaction with temporally shaped femtosecond laser pulses: experiments and simulations*, Appl. Surf. Sci. (In Press).
29. T. Q. Jia, H. X. Chen, M. Huang, F. L. Zhao, X. X. Li, S. Z. Xu, H. Y. Sun, D. H. Feng, C. B. Li, X. F. Wang, R. X. Li, Z. Z. Xu, X. K. He, and H. Kuroda, *Ultraviolet-infrared femtosecond laser-induced damage in fused silica and CaF2 crystals*, Phys. Rev. B **73**(2006).
30. D. Puerto, J. Siegel, W. Gawelda, M. Galvan-Sosa, L. Ehrentraut, J. Bonse, and J. Solis, *Dynamics of plasma formation, relaxation, and topography modification induced by femtosecond laser pulses in crystalline and amorphous dielectrics*, J. Opt. Soc. Am. B. **27**, 1065 (2010).
31. K. Waedegaard, M. Frislev, and P. Balling, *Femtosecond laser excitation of dielectric materials: experiments and modeling of optical properties and ablation depths*, Appl. Phys. A **110**, 601 (2013).
32. A. Dubietis, A. Couairon, E. Kucinskas, G. Tamosauskas, E. Gaizauskas, D. Faccio, and P. Di Trapani, *Measurement and calculation of nonlinear absorption associated with femtosecond filaments in water*, Appl. Phys. B **84**, 439 (2006).
33. A. Kaiser, B. Rethfeld, M. Vicanek, and G. Simon, *Microscopic processes in dielectrics under irradiation by subpicosecond laser pulses*, Phys. Rev. B **61**, 11437 (2000).
34. D. Grojo, S. Leyder, P. Delaporte, W. Marine, M. Sentis, and O. Uteza, *Long-wavelength multiphoton ionization inside band-gap solids*, Phys. Rev. B **88**(2013).
35. B. Rethfeld, *Unified model for the free-electron avalanche in laser-irradiated dielectrics*, Phys. Rev. Lett. **92**, 187401 (2004).
36. B. Rethfeld, *Free-electron generation in laser-irradiated dielectrics*, Phys. Rev. B **73**, 035101 (2006).
37. A. C. Tien, S. Backus, H. Kapteyn, M. Murnane, and G. Mourou, *Short-pulse laser damage in transparent materials as a function of pulse duration*, Phys. Rev. Lett. **82**, 3883 (1999).
38. B. Rethfeld, O. Brenk, N. Medvedev, H. Krutsch, and D. H. H. Hoffmann, *Interaction of dielectrics with femtosecond laser pulses: Application of kinetic approach and multiple rate equation*, Appl. Phys. A **101**, 19 (2010).
39. B. H. Christensen and P. Balling, *Modeling ultrashort-pulse laser ablation of dielectric materials*, Phys. Rev. B **79**(2009).
40. D. Du, X. Liu, G. Korn, J. Squier, and G. Mourou, *Laser-Induced Breakdown by Impact Ionization in Sio2 with*

Pulse Widths from 7 Ns to 150 Fs, Appl. Phys. Lett. **64**, 3071 (1994).

41. A. P. Joglekar, H. Liu, G. J. Spooner, E. Meyhofer, G. Mourou, and A. J. Hunt, *A study of the deterministic character of optical damage by femtosecond laser pulses and applications to nanomachining*, Appl. Phys. B **77**, 25 (2003).
42. A. P. Joglekar, H. H. Liu, E. Meyhofer, G. Mourou, and A. J. Hunt, *Optics at critical intensity: Applications to nanomorphing*, Proc. Natl. Acad. Sci. U.S.A. **101**, 5856 (2004).
43. D. Du, X. Liu, and G. Mourou, *Reduction of multi-photon ionization in dielectrics due to collisions*, Appl. Phys. B **63**, 617 (1996).
44. A. Vaidyanathan, T. W. Walker, and A. H. Guenther, *Relative roles of avalanche multiplication and multiphoton absorption in laser-induced damage of dielectrics*, IEEE J. Quantum Electron. **16**, 89 (1980).
45. M. V. Ammosov, N. B. Delone, and V. P. Krainov, *Tunnel ionization of complex atoms and atomic ions in a varying electromagnetic-field*, Zh. Eksp. Teor. Fiz. **91**, 2008 (1986).
46. M. Jupe, L. Jensen, A. Melninkaitis, V. Sirutkaitis, and D. Ristau, *Calculations and experimental demonstration of multi-photon absorption governing fs laser-induced damage in titania*, Opt. Express **17**, 12269 (2009).
47. L. Gallais, D. B. Douti, M. Commandre, G. Bataviciute, E. Pupka, M. Sciuka, L. Smalakys, V. Sirutkaitis, and A. Melninkaitis, *Wavelength dependence of femtosecond laser-induced damage threshold of optical materials*, J. Appl. Phys. **117**(2015).
48. D. M. Simanovskii, H. A. Schwettman, H. Lee, and A. J. Welch, *Midinfrared optical breakdown in transparent dielectrics*, Phys. Rev. Lett. **91**(2003).
49. G. Olivie, D. Giguere, F. Vidal, T. Ozaki, J. C. Kieffer, O. Nada, and I. Brunette, *Wavelength dependence of femtosecond laser ablation threshold of corneal stroma*, Opt. Express **16**, 4121 (2008).
50. C. B. Schaffer, A. Brodeur, J. F. García, and E. Mazur, *Micromachining bulk glass by use of femtosecond laser pulses with nanojoule energy*, Opt. Lett. **26**, 93 (2001).
51. A. Vogel, N. Linz, S. Freidank, and G. Paltauf, *Femtosecond laser induced nanocavitation in water: implications for optical breakdown threshold and cell surgery*, Phys. Rev. Lett. **100**, 038102 (2008).
52. L. Sudrie, A. Couairon, M. Franco, B. Lamouroux, B. Prade, S. Tzortzakis, and A. Mysyrowicz, *Femtosecond laser-induced damage and filamentary propagation in fused silica*, Phys. Rev. Lett. **89**(2002).
53. D. J. Stevenson, F. J. Gunn-Moore, P. Campbell, and K. Dholakia, *Single cell optical transfection*, J. R. Soc. Interface **7**, 863 (2010).
54. H. Lubatschowski, *Overview of commercially available femtosecond lasers in refractive surgery*, J. Refract. Surg. **24**, 102 (2008).
55. R. Le Harzic, K. Konig, C. Wullner, K. Vogler, and C. Donitzky, *Ultraviolet femtosecond laser creation of corneal flap*, J. Refract. Surg. **25**, 383 (2009).
56. C. M. Hammer, C. Petsch, J. Klenke, K. Skerl, F. Paulsen, F. E. Kruse, T. Seiler, and J. Menzel-Severing, *Corneal tissue interactions of a new 345 nm ultraviolet femtosecond laser*, J. Cataract. Refr. Surg. **41**, 1279 (2015).
57. J. Wang, G. Schuele, and D. Palanker, *Finesse of transparent tissue cutting by ultrafast lasers at various wavelengths*, J. Biomed. Opt. **20**, 125004 (2015).
58. A. Vogel, S. Freidank, and N. Linz, "IR and UV vortex beams for ultraprecise plasma-mediated eye surgery," (SPIE Newsroom, DOI: 10.1117/2.1201511.006157, 2016).
59. Z. S. Sacks, R. M. Kurtz, T. Juhasz, G. Spooner, and G. A. Mouroua, *Subsurface photodisruption in human sclera: wavelength dependence*, Ophthalmic Surg. Lasers Imaging **34**, 104 (2003).
60. L. Habbema, R. Verhagen, R. Van Hal, Y. Liu, and B. Varghese, *Minimally invasive non-thermal laser technology using laser-induced optical breakdown for skin rejuvenation*, J. Biophotonics **5**, 194 (2012).
61. J. Z. Qiu, J. Neev, T. Y. Wang, and T. E. Milner, *Deep subsurface cavities in skin utilizing mechanical optical*

clearing and femtosecond laser ablation, Laser Surg. Med. **45**, 383 (2013).

62. M. Yildirim, O. Ferhanoglu, J. Kobler, S. M. Zeitels, and A. Ben-Yakar, *Parameters affecting ultrafast laser microsurgery of subepithelial voids for scar treatment in vocal folds*, J. Biomed. Opt. **18**(2013).
63. Z. S. Sacks, R. M. Kurtz, T. Juhasz, and G. A. Mourou, "Femtosecond subsurface photodisruption in scattering human tissues using long infrared wavelengths," in *Proc. SPIE 4241, Saratov Fall Meeting 2000: Optical Technologies in Biophysics and Medicine II*, 2001),
64. K. Plamann, F. Aptel, C. L. Arnold, A. Courjaud, C. Crotti, F. Deloison, F. Druon, P. Georges, M. Hanna, J. M. Legeais, F. Morin, E. Mottay, V. Nuzzo, D. A. Peyrot, and M. Savoldelli, *Ultrashort pulse laser surgery of the cornea and the sclera*, J. Opt. **12**(2010).
65. C. Xu and F. W. Wise, *Recent advances in fibre lasers for nonlinear microscopy*, Nat. Photonics **7**, 1006 (2013).
66. "Light Conversion homepage: http://www.lightcon.com/."
67. A. Vogel, J. Noack, K. Nahen, D. Theisen, S. Busch, U. Parlitz, D. X. Hammer, G. D. Noojin, B. A. Rockwell, and R. Birngruber, *Energy balance of optical breakdown in water at nanosecond to femtosecond time scales*, Appl. Phys. B. **68**, 271 (1999).
68. C. Schaffer, N. Nishimura, E. Glezer, A. Kim, and E. Mazur, *Dynamics of femtosecond laser-induced breakdown in water from femtoseconds to microseconds*, Opt. Express **10**, 196 (2002).
69. N. M. Bulgakova, V. P. Zhukov, S. V. Sonina, and Y. P. Meshcheryakov, *Modification of transparent materials with ultrashort laser pulses: What is energetically and mechanically meaningful?*, J. Appl. Phys. **118**(2015).
70. C. L. Thomsen, D. Madsen, S. R. Keiding, J. Thogersen, and O. Christiansen, *Two-photon dissociation and ionization of liquid water studied by femtosecond transient absorption spectroscopy*, J. Chem. Phys. **110**, 3453 (1999).
71. C. G. Elles, A. E. Jailaubekov, R. A. Crowell, and S. E. Bradforth, *Excitation-energy dependence of the mechanism for two-photon ionization of liquid H2O and D2O from 8.3 to 12.4 eV*, J. Chem. Phys. **125**, 044515 (2006).
72. C. G. Elles, C. A. Rivera, Y. Zhang, P. A. Pieniazek, and S. E. Bradforth, *Electronic structure of liquid water from polarization-dependent two-photon absorption spectroscopy*, J. Chem. Phys. **130**, 084501 (2009).
73. J. L. Li, Z. G. Nie, Y. Y. Zheng, S. Dong, and Z. H. Loh, *Elementary electron and ion dynamics in ionized liquid water*, J. Phys. Chem. Lett. **4**, 3698 (2013).
74. J. W. Boyle, J. A. Ghormley, Hochanad.Cj, and J. R. Riley, *Production of hydrated electrons by flash photolysis of liquid water with light in first continuum*, J. Phys. Chem. **73**, 2886 (1969).
75. F. Williams, S. P. Varma, and S. Hillenius, *Liquid water as a lone-pair amorphous semiconductor*, J. Chem. Phys. **64**, 1549 (1976).
76. D. N. Nikogosyan, A. A. Oraevsky, and V. I. Rupasov, *Two-photon ionization and dissociation of liquid water by powerful laser UV radiation*, Chem. Phys. **77**, 131 (1983).
77. D. M. Bartels and R. A. Crowell, *Photoionization yield vs energy in H2O and D2O*, J. Phys. Chem. A **104**, 3349 (2000).
78. L. Kevan, *Solvated electron-structure in glassy matrices*, Accounts Chem. Res. **14**, 138 (1981).
79. M. S. Pshenichnikov, A. Baltuska, and D. A. Wiersma, *Hydrated-electron population dynamics*, Chem. Phys. Lett. **389**, 171 (2004).
80. A. Thaller, R. Laenen, and A. Laubereau, *Femtosecond spectroscopy of the hydrated electron: novel features in the infrared*, Chem. Phys. Lett. **398**, 459 (2004).
81. J. Savolainen, F. Uhlig, S. Ahmed, P. Hamm, and P. Jungwirth, *Direct observation of the collapse of the delocalized excess electron in water*, Nat. Chem. **6**, 697 (2014).
82. R. A. Crowell and D. M. Bartels, *Multiphoton ionization of liquid water with 3.0-5.0 eV photons*, J. Phys.

Chem. **100**, 17940 (1996).

83. R. Lian, D. A. Oulianov, I. A. Shkrob, and R. A. Crowell, *Geminate recombination of electrons generated by above-the-gap (12.4 eV) photoionization of liquid water*, Chem. Phys. Lett. **398**, 102 (2004).
84. C. G. Elles, I. A. Shkrob, R. A. Crowell, and S. E. Bradforth, *Excited state dynamics of liquid water: Insight from the dissociation reaction following two-photon excitation*, J. Chem. Phys. **126**(2007).
85. F. Uhlig, O. Marsalek, and P. Jungwirth, *Unraveling the complex nature of the hydrated electron*, J. Phys. Chem. Lett. **3**, 3071 (2012).
86. A. Kumar, J. A. Walker, D. M. Bartels, and M. D. Sevilla, *A simple ab initio model for the hydrated electron that matches experiment*, J. Phys. Chem. A **119**, 9148 (2015).
87. R. A. Crowell, R. Lian, I. A. Shkrob, J. Qian, D. A. Oulianov, and S. Pommeret, *Light-induced temperature jump causes power-dependent ultrafast kinetics of electrons generated in multiphoton ionization of liquid water*, J. Phys. Chem. A **108**, 9105 (2004).
88. A. Migus, Y. Gauduel, J. L. Martin, and A. Antonetti, *Excess electrons in liquid water - First evidence of a prehydrated state with femtosecond lifetime*, Phys. Rev. Lett. **58**, 1559 (1987).
89. M. Assel, R. Laenen, and A. Laubereau, *Femtosecond solvation dynamics of solvated electrons in neat water*, Chem. Phys. Lett. **317**, 13 (2000).
90. S. Minardi, C. Milian, D. Majus, A. Gopal, G. Tamosauskas, A. Couairon, T. Pertsch, and A. Dubietis, *Energy deposition dynamics of femtosecond pulses in water*, Appl. Phys. Lett. **105**(2014).
91. S. Minardi, A. Gopal, M. Tatarakis, A. Couairon, G. Tamosauskas, R. Piskarskas, A. Dubietis, and P. Di Trapani, *Time-resolved refractive index and absorption mapping of light-plasma filaments in water*, Opt. Lett. **33**, 86 (2008).
92. L. V. Keldysh, *Ionization in the field of a strong electromagnetic wave*, Sov. Phys. Jetp. **20**, 1307 (1965).
93. D. H. Son, P. Kambhampati, T. W. Kee, and P. F. Barbara, *Delocalizing electrons in water with light*, J. Phys. Chem. A **105**, 8269 (2001).
94. L. V. Keldysh, *Kinetic theory of impact ionization in semiconductors*, Sov. Phys. Jetp. **10**, 509 (1960).
95. B. K. Ridley, *Quantum processes in semiconductors* (Clarendon Press, Oxford, 1999).
96. D. Arnold and E. Cartier, *Theory of laser-induced free-electron heating and impact ionization in wide-band-gap solids*, Phys. Rev. B **46**, 15102 (1992).
97. N. Brouwer and B. Rethfeld, *Excitation and relaxation dynamics in dielectrics irradiated by an intense ultrashort laser pulse*, J. Opt. Soc. Am. B. **31**, C28 (2014).
98. A. Ramer, O. Osmani, and B. Rethfeld, *Laser damage in silicon: Energy absorption, relaxation, and transport*, J. Appl. Phys. **116**(2014).
99. D. Hulin, M. Combescot, J. Bok, A. Migus, J. Y. Vinet, and A. Antonetti, *Energy-transfer during silicon irradiation by femtosecond laser-pulse*, Phys. Rev. Lett. **52**, 1998 (1984).
100. C. DeMichelis, *Laser induced gas breakdown - a bibliographical review*, IEEE J. Quantum Electron. **Qe 5**, 188 (1969).
101. K. Sokolowski-Tinten and D. von der Linde, *Generation of dense electron-hole plasmas in silicon*, Phys. Rev. B **61**, 2643 (2000).
102. K. Starke, D. Ristau, H. Welling, T. V. Amotchkina, M. Trubetskov, A. A. Tikhonravov, and A. S. Chirkin, "Investigations in the nonlinear behavior of dielectrics by using ultrashort pulses (Best Oral Presentation)," in *Proc. SPIE 5273, Laser-Induced Damage in Optical Materials: 2003, 501*, 2004), 501.
103. M. D. Feit, A. M. Komashko, and A. M. Rubenchik, *Ultra-short pulse laser interaction with transparent dielectrics*, Appl. Phys. A **79**, 1657 (2004).
104. M. Grundmann, *The physics of semiconductors : an introduction including nanophysics and applications,* 2nd ed., Graduate texts in physics, (Springer-Verlag, Berlin; New York, 2010).

105. F. Docchio, *Lifetimes of plasmas induced in liquids and ocular media by single Nd-YAG laser-pulses of different duration*, Europhys. Lett. **6**, 407 (1988).
106. J. Urbanek, "Multiphoton ionization and recombination dynamics in liquid-to-supercritical ammonia," (University of Bonn, Bonn, 2014).
107. A. Seilmeier and W. Kaiser, *Ultrashort intramolecular and intermolecular vibrational energy transfer of polyatomic molecules in liquids*, in Ultrashort Laser Pulses, edited by W. Kaiser (Springer-Verlag, Berlin; Heidelberg, 1993).
108. S. Woutersen and H. J. Bakker, *Resonant intermolecular transfer of vibrational energy in liquid water*, Nature **402**, 507 (1999).
109. M. L. Cowan, B. D. Bruner, N. Huse, J. R. Dwyer, B. Chugh, E. T. J. Nibbering, T. Elsaesser, and R. J. D. Miller, *Ultrafast memory loss and energy redistribution in the hydrogen bond network of liquid H2O*, Nature **434**, 199 (2005).
110. J. Lindner, P. Vohringer, M. S. Pshenichnikov, D. Cringus, D. A. Wiersma, and M. Mostovoy, *Vibrational relaxation of pure liquid water*, Chem. Phys. Lett. **421**, 329 (2006).
111. D. Nordlund, H. Ogasawara, H. Bluhm, O. Takahashi, M. Odelius, M. Nagasono, L. G. M. Pettersson, and A. Nilsson, *Probing the electron delocalization in liquid water and ice at attosecond time scales*, Phys. Rev. Lett. **99**(2007).
112. C. L. Arnold, A. Heisterkamp, W. Ertmer, and H. Lubatschowski, *Computational model for nonlinear plasma formation in high NA micromachining of transparent materials and biological cells*, Opt. Express **15**, 10303 (2007).
113. L. Englert, B. Rethfeld, L. Haag, M. Wollenhaupt, C. Sarpe-Tudoran, and T. Baumert, *Control of ionization processes in high band gap materials via tailored femtosecond pulses*, Opt. Express **15**, 17855 (2007).
114. D. Bolmatov, V. V. Brazhkin, and K. Trachenko, *The phonon theory of liquid thermodynamics*, Sci. Rep. **2**(2012).
115. Q. Sun, H. B. Jiang, Y. Liu, Z. X. Wu, H. Yang, and Q. H. Gong, *Measurement of the collision time of dense electronic plasma induced by a femtosecond laser in fused silica*, Opt. Lett. **30**, 320 (2005).
116. P. N. Saeta and B. I. Greene, *Primary relaxation processes at the band-edge of SiO2*, Phys. Rev. Lett. **70**, 3588 (1993).
117. P. Audebert, P. Daguzan, A. Dossantos, J. C. Gauthir, J. P. Geindre, S. Guizard, G. Hamoniaux, K. Krastev, P. Martin, G. Petite, and A. Antonetti, *Space-time observation of an electron-gas in SiO2*, Phys. Rev. Lett. **73**, 1990 (1994).
118. P. Martin, S. Guizard, P. Daguzan, G. Petite, P. D'Oliveira, P. Meynadier, and M. Perdrix, *Subpicosecond study of carrier trapping dynamics in wide-band-gap crystals*, Phys. Rev. B **55**, 5799 (1997).
119. A. Zoubir, M. Richardson, L. Canioni, A. Brocas, and L. Sarger, *Optical properties of infrared femtosecond laser-modified fused silica and application to waveguide fabrication*, J. Opt. Soc. Am. B. **22**, 2138 (2005).
120. K. H. Zhang, L. Jiang, X. Li, X. S. Shi, D. Yu, L. T. Qu, and Y. F. Lu, *Femtosecond laser pulse-train induced breakdown in fused silica: the role of seed electrons*, J. Phys. D **47**, 435105 (2014).
121. A. A. Oraevsky and D. N. Nikogosyan, *Picosecond two-quantum UV photochemistry of thymine in aqueous solution*, Chem. Phys. **100**, 429 (1985).
122. D. N. Nikogosyan and H. Görner, *Towards the laser photochemistry of the cornea: studies of the most common and highly absorbing aliphatic amino acids in collagen*, Journal of Photochemistry and Photobiology B: Biology **47**, 63 (1998).
123. D. N. Nikogosyan and H. Görner, *Laser-induced photodecomposition of amino acids and peptides: extrapolation to corneal collagen*, IEEE J. Sel. Topics Quantum Electron. **5**, 1107 (1999).
124. C. Eggeling, A. Volkmer, and C. A. M. Seidel, *Molecular photobleaching kinetics of rhodamine 6G by one-*

and two-photon induced confocal fluorescence microscopy, ChemPhysChem **6**, 791 (2005).

125. V. Hovhannisyan, W. Lo, C. Hu, S.-J. Chen, and C. Y. Dong, *Dynamics of femtosecond laser photo-modification of collagen fibers*, Opt. Express **16**, 7958 (2008).
126. V. Hovhannisyan, A. Ghazaryan, Y.-F. Chen, S.-J. Chen, and C.-Y. Dong, *Photophysical mechanisms of collagen modification by 80 MHz femtosecond laser*, Opt. Express **18**, 24037 (2010).
127. R. Orzekowsky-Schroeder, A. Klinger, B. Martensen, M. Blessenohl, A. Gebert, A. Vogel, and G. Huttmann, *In vivo spectral imaging of different cell types in the small intestine by two-photon excited autofluorescence*, J. Biomed. Opt. **16**(2011).
128. R. Galli, O. Uckermann, E. F. Andresen, K. D. Geiger, E. Koch, G. Schackert, G. Steiner, and M. Kirsch, *Intrinsic indicator of photodamage during label-free multiphoton microscopy of cells and tissues*, PLoS ONE **9**, e110295 (2014).
129. D. Débarre, N. Olivier, W. Supatto, and E. Beaurepaire, *Mitigating phototoxicity during multiphoton microscopy of live drosophila embryos in the 1.0–1.2 µm wavelength range*, PLoS ONE **9**, e104250 (2014).
130. R. Orzekowsky-Schroeder, A. Klinger, S. Freidank, N. Linz, S. Eckert, G. Hüttmann, A. Gebert, and A. Vogel, *Probing the immune and healing response of murine intestinal mucosa by time-lapse 2-photon microscopy of laser-induced lesions with real-time dosimetry*, Biomed. Opt. Express **5**, 3521 (2014).
131. J. Wang, G. Schuele, P. Huie, and D. V. Palanker, "Role of molecular photodissociation in ultrafast laser surgery," in 2015), 932107.
132. N. Nishimura, C. B. Schaffer, B. Friedman, P. S. Tsai, P. D. Lyden, and D. Kleinfeld, *Targeted insult to subsurface cortical blood vessels using ultrashort laser pulses: three models of stroke*, Nat. Methods **3**, 99 (2006).
133. J. Nguyen, J. Ferdman, M. R. Zhao, D. Huland, S. Saqqa, J. Ma, N. Nishimura, T. H. Schwartz, and C. B. Schaffer, *Sub-surface, micrometer-scale incisions produced in rodent cortex using tightly-focused femtosecond laser pulses*, Laser Surg. Med. **43**, 382 (2011).
134. A. Trost, F. Schroedl, C. Strohmaier, B. Bogner, C. Runge, A. Kaser-Eichberger, K. Krefft, A. Vogel, N. Linz, S. Freidank, A. Hilpert, I. Zimmermann, G. Grabner, and H. A. Reitsamer, *A new nanosecond UV laser at 355 nm: Early results of corneal flap cutting in a rabbit model*, Invest. Ophthalmol. Vis. Sci. **54**, 7854 (2013).
135. S. L. Jacques, *Optical properties of biological tissues: a review*, Phys. Med. Biol. **58**, 5007 (2013).